Int J Adv Manuf Technol (2015) 80:65–90
DOI 10.1007/s00170-015-6958-9

ORIGINAL ARTICLE

5-axis machining using a curvilinear tool path aligned with the direction of the maximum removal rate

S. Moodleah · S. S. Makhanov

Received: 9 July 2014 / Accepted: 23 February 2015 / Published online: 18 March 2015

Abstract Machining large complex industrial parts with a high accuracy often requires tens, hundreds of thousands, or even millions of cutter location points and hundreds of hours of machining. That is why reducing the machining time is one of the most important topics in the optimization of CNC codes for 5-axis milling machines. We propose and analyze a new method of constructing curvilinear tool paths which partly or even entirely align with the direction of the maximum material removal rate. The alignment based on the curvilinear elliptic grid generation allows minimization of the machining time while keeping the convenient zigzag-like topology of the path. The method is applicable to a variety of cost functions such as the length of the path, the machining speed, the material removal rate, the kinematic error, etc., generating different machining strategies. The method has been combined with a new version of the adaptive space-filling curves. The approach has been tested against the standard iso-parametric zigzag, MasterCamX5, "Follow Periphery"/"Helical or Spiral" options of Unigraphics as well as the conventional space-filling curves. The material removal rate cost function has been tested against the tool path length minimization. The numerical and machining experiments demonstrate a considerable advantage of the proposed method.

Keywords Kinematics of the milling machines · Error minimization · Tool path planning

S. Moodleah · S. S. Makhanov (✉)
School of Information, Computer and Communication Technology,
Sirindhorn International Institute of Technology,
Thammasat University, Pathum Thani, Thailand
e-mail: makhanov@siit.tu.ac.th

1 Introduction

Milling machines designed for cutting complex industrial parts consist of several mechanical blocks to establish the required coordinates and orientations of the tool during the cutting process. The machine is guided by a controller which is fed with the CNC program or G-code. The code is a sequence of commands carrying three spatial coordinates of the tool tip and a pair of rotation angles needed to establish the orientation of the tool. The G-code is a set of the Cartesian coordinates of the cutter location points (CL points) in the machine coordinate system and the tool orientation vectors. The rotation angles are functions of the tool orientations. The configuration of a 5-axis milling machine is characterized by

- Rotation matrices A and B corresponding to the two rotary axes,
- Translations T_{23} and T_{34}, where T_{23} is the coordinate of the center of the A-axis in the B-axis coordinate system and T_{34}, the coordinate of the center of the B-axis in the spindle coordinate system,
- Length of the tool L treated as an additional translation T_4 (T_4=(0, 0, L) or (0, 0, −L)) depending on the direction of the tool tip in the spindle coordinate system.

Figures 1, 2, 3, and 4 display two configurations used in this study.

The tool path optimization problem is usually formulated in terms of a combination of measures of the machining efficiency. Typically, such measures are the difference between the required and the output surface (accuracy), the length of the tool path, the negative of the machining strip (strip maximization), the machining time, etc. [1, 2].

The tool path planning methods solve this problem by generating a connected set of the positions and orientations of the cutting tool in the workpiece coordinate system. Technically,

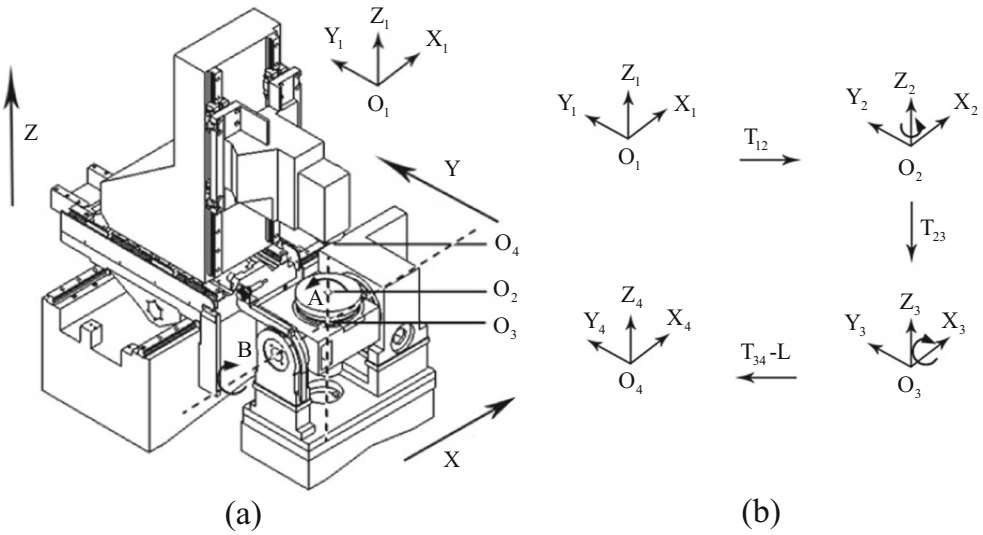

Fig. 1 5-axis milling machine with the rotary axes on the table

the positions of the tool do not need to follow any rigid geometrical pattern; however, the standard manufacturing tool paths follow the zigzag or the spiral pattern. Recently proposed patterns are the Hilbert space-filling curves [3–8] and the adaptive space-filling curves [9–13].

The optimization could be subjected to constraints, the most important of which is the machining accuracy. In this paper, the accuracy is evaluated by measuring the scallop heights and the kinematic error [14–19].

The scallop heights are kept within the allowable range by evaluating the machining strip and selecting an appropriate offset between the adjacent tool tracks. Larger machining strips allow for a larger distance between the tracks, reducing the number of tracks and consequently, the length of the tool path. When the tool is inclined to match the surface curvature, it is desirable that the tool follows a direction such that the curvature to be matched is minimal. The smaller the curvature is, the smaller the required inclination angle is and the larger the machining strip is, thus decreasing the tool path. Unfortunately, the time reduction problem is not that straightforward. The actual machining time depends on the tool path in the machine coordinates rather than in the workpiece coordinates. Therefore, minimization of the machining time is a machine-dependent problem whereas minimization of the tool path length can be treated as the machine-independent problem.

Fig. 2 Haas VF-2TR, National Institute of Metrology, Thailand

Let us consider a part surface, discretize it, and at every point, evaluate a direction (vector) of the maximum material removal rate. The collection of the vectors constitutes a vector field defined in the parametric coordinates. We will call a tool path which visits every point, follows the desired vector field at every point, and does not self intersect the optimal tool path. Constructing such a tool path is a difficult task. First attempts to optimize the tool path relative to a certain vector field are the non-iso-parametric tool paths [20, 21] and the iso-scallop tool path [1] proposed by C.C. Lo. The tool path is generated by an adaptive offsetting an initial curve (usually a boundary) so that the maximum machining strip or a maximum allowable scallop height is achieved along the offset curve. For instance, the iso-scallop algorithm searches for a set of points which lie next to the initial curve and satisfy the scallop constraint; the resulting points are then connected to generate the next track of the tool.

An efficient algorithm to find a suboptimal solution of the tool path aligned with the vector field is presented in [22]. The entire surface is discretized using a rectangular grid in the parametric space and then covered by potential machining patches, each characterized by one or several optimal directions producing the maximum machining strip (Fig. 5).

The method requires an "initial path" which has the largest average machining strip. The entire tool path is

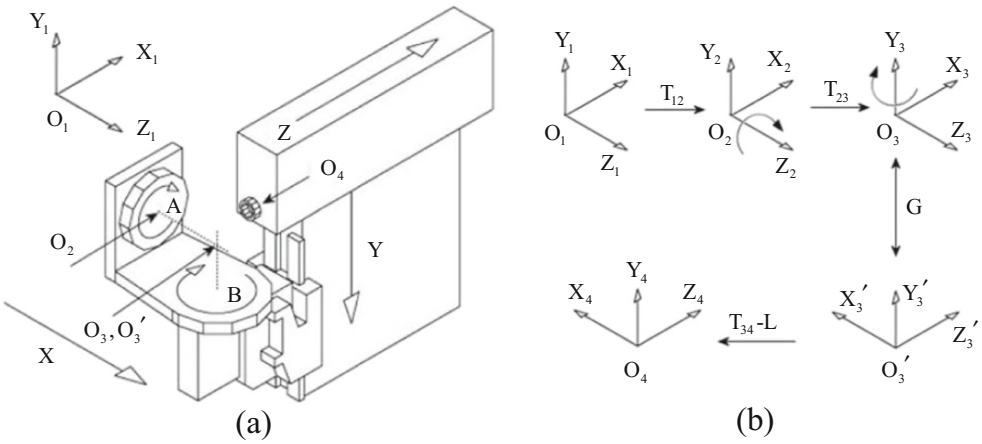

Fig. 3 5-axis milling machine with rotary axes on the table

constructed by offsetting the initial path and propagating the offsets inside the region. The offset tracks are modified if they substantially deviate from the streamlines of the optimal directions. In other words, at some point, the algorithm generates a new initial track.

Unfortunately, many surfaces produce a complicated, non-uniform vector field and although the above algorithm allows one to decompose the surface into sub-surfaces, the decomposition is not very well motivated from the optimization viewpoint. In particular, after the first propagation step, the algorithm searches for a new "initial tool path" such that the ratio between the length of the path and the average machining strip is less than a certain threshold. It is not hard to show that such analysis is not always accurate from the viewpoint of global optimization. It may also be sensitive to local variations of the optimization criteria. Moreover, finding the initial tool path is a computationally expensive, non-deterministic polynomial time (NP)-hard problem. Finally, additional efforts must be made to ensure that the resulting tool path is structured, that is, becomes a zigzag or spiral.

Fig. 4 MAHO 600 E, Asian Institute of Technology, Thailand

The vector field of the optimal tool directions to capture the "skeletal" information of tool path (or a family of a tool paths) can be combined with the geometric constraints, evaluation of the kinematic performance of the machine, and other constraints such as the cutting force limits [23, 24]. However, solutions of such problems are still purely heuristic due to the high computational complexity.

The surface can be partitioned into clusters so that the streamlines of the vector field are close to the conventional zigzag or spiral [25, 26]. Within a cluster, the tool follows a nearly optimal path. Clustering optimizes a global criterion of the decomposition and makes it possible not only to decompose the surface but also to recognize similarities to the conventional tool path patterns. Although an appropriate linking of the clusters can be performed [27], a complicated vector field often produces too many clusters. Besides, the partition requires tool withdrawals which increase the machining time. More importantly, the surface smoothness at the connecting boundaries can be jeopardized.

Finally, following the optimal or nearly optimal directions can be combined with rear gouging, global gouging, and machine limits constraints. For instance, the accessibility map [28], composed of the admissible ranges of the inclination and yaw angles is combined with a smoothness map measured by the derivatives of the tool vectors evaluated at the prescribed cutter location points. The two maps are employed by a path propagation algorithm similar to [22]. However, the algorithm also requires an initial track. Besides, the smoothness map [28] is not efficient from the kinematic error viewpoint. For instance, the stationary points of the surface may invoke large variations of the rotation angles [29] and large kinematic errors; however, the smoothness map does not take into account this effect.

We propose to construct a curvilinear tool path aligned with the optimal vector field using the elliptic grid generation. The optimal directions are evaluated using the maximum material removal rate rather than the length of the tool path as in [22]. The resulting vector field-aligned path

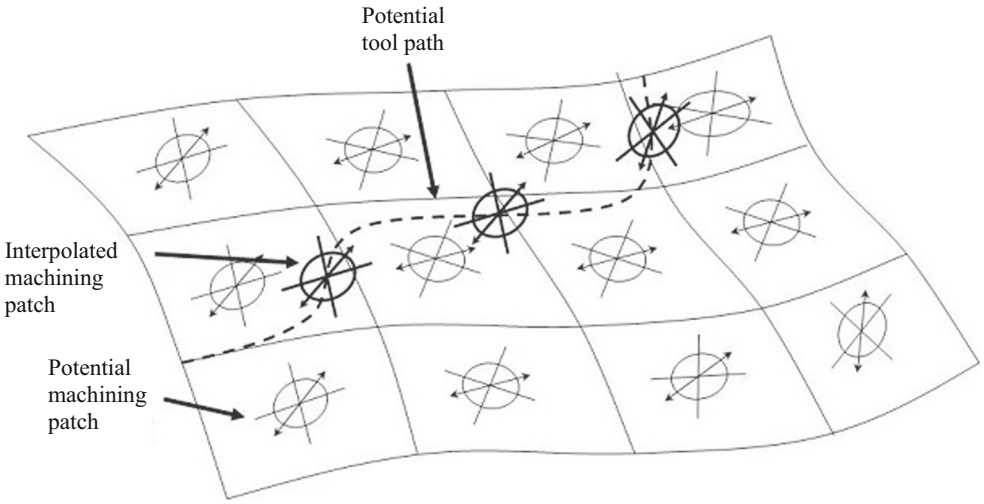

Fig. 5 Potential vector field

(VFAP) is a compromise between the flexibility of methods based on propagating of the initial track and the simplicity of the zigzag topology. The proposed method extends the research on grid generation for 5-axis machining originally proposed in [26, 30–32] and independently in [33].

The curvilinear grid [34, 35] is aligned with the optimal cutting directions represented by a pre-computed vector field. The grid is generated in the parametric domain and does not require an initialization. In contrast, the initial tool path [28] is a computationally expensive NP-hard problem. Although good initializations can lead to a substantial decrease in the tool path length [22], the sensitivity of the method to the initial path (or even the initial point) could be high. Some initial curves may not lead to any improvement in the machining time at all. The grid generation method, on the other hand, always leads to the same result. Besides, the method is based on the material removal rate rather than on the tool path length minimization. That is the second reason for its efficiency and reliability.

In order to reduce the kinematic error, we combine the aligned path with a new modification of the space-filling curves [9, 13] (see Appendix A) called the biased space-filling curve (BSFC). The BSFC follows the optimal directions and reduces the frequent turns typically generated by conventional space-filling curves (SFC) at the expense of a slight decrease of the machining time.

The combination of VFAP based on the material removal rate and the BSFC is the main contribution of this paper.

2 Maximum material removal rate. Vector field of the optimal directions

Let W_1 be an arbitrary cutter contact (CC) point on the surface (Fig. 6). Consider a set of points on the surface defined by $\Omega_{W_1} = \{W : \mathrm{dist}_S(W_1, W) = l_1\}$, where dist_S is the geodesic distance and l_1 is a small prescribed step (see Fig. 6a). The corresponding set of points in the machine coordinates is denoted by Ω_{M_1}. The distance between the corresponding points is given by $l_{1,M} \equiv l_{1,M}(W)$. The machining strip corresponding to the feed direction $\overrightarrow{W_1, W}$ is denoted by $w_1 \equiv w_1(W)$. Figure 6b exemplifies Ω_{W_1} and Ω_{M_1} for a surface depicted in Fig. 6a obtained by the inverse kinematic transformations of Haas VF-2TR (Figs. 1 and 2). Note that Ω_{W_1} is approximately a circle, whereas Ω_{M_1} is an irregular, ellipse-shaped, closed curve. Clearly, equal increments on the surface (in the workpiece coordinate system) do not lead to equal increments in the machine coordinates. Therefore, the machining time depends critically on the translations in the machine coordinates rather than in the workpiece coordinates.

Furthermore, introduce an instantaneous material removal rate in the direction $\overrightarrow{W_1, W}$ given by $R_M(W) = \frac{F\, l_1(W) w_1(W)}{l_{1,M}}$, where F is the feed rate. The machining strip w_1 corresponding to the prescribed feed direction is evaluated by locating the intersections of the effective cutting shape and the design surface (see [13] for details).

Note that the machining strip depends on the shape of the tool (ball nose, flat end, toroidal end mill, etc.) and its inclination. For instance, the flat-end tool must be inclined to avoid gouging and curvature interference. Therefore, $R_M(W)$ includes the tool shape and inclination. Since, the type of the tool and the tool vector are implicitly included, the algorithm works for any type of the tool and any strategy to avoid gouging and the curvature interference.

We will call the direction $\overrightarrow{W_1, W_2}$ optimal if $W_2 = \mathrm{argmax}_{W \in \Omega_{W_1}} R_M(W)$. In other words, if W_2 maximizes the material removal rate. Evaluating vectors $\overrightarrow{W_1, W_2}$ for each surface point and transferring them into the parametric domain (u,v) generates the vector field $V(u,v) \equiv (v_x(u,v), v_y(u,v))$.

Note that the rotation angles are also implicitly involved in the maximization of R_M as follows. Let us assume that the

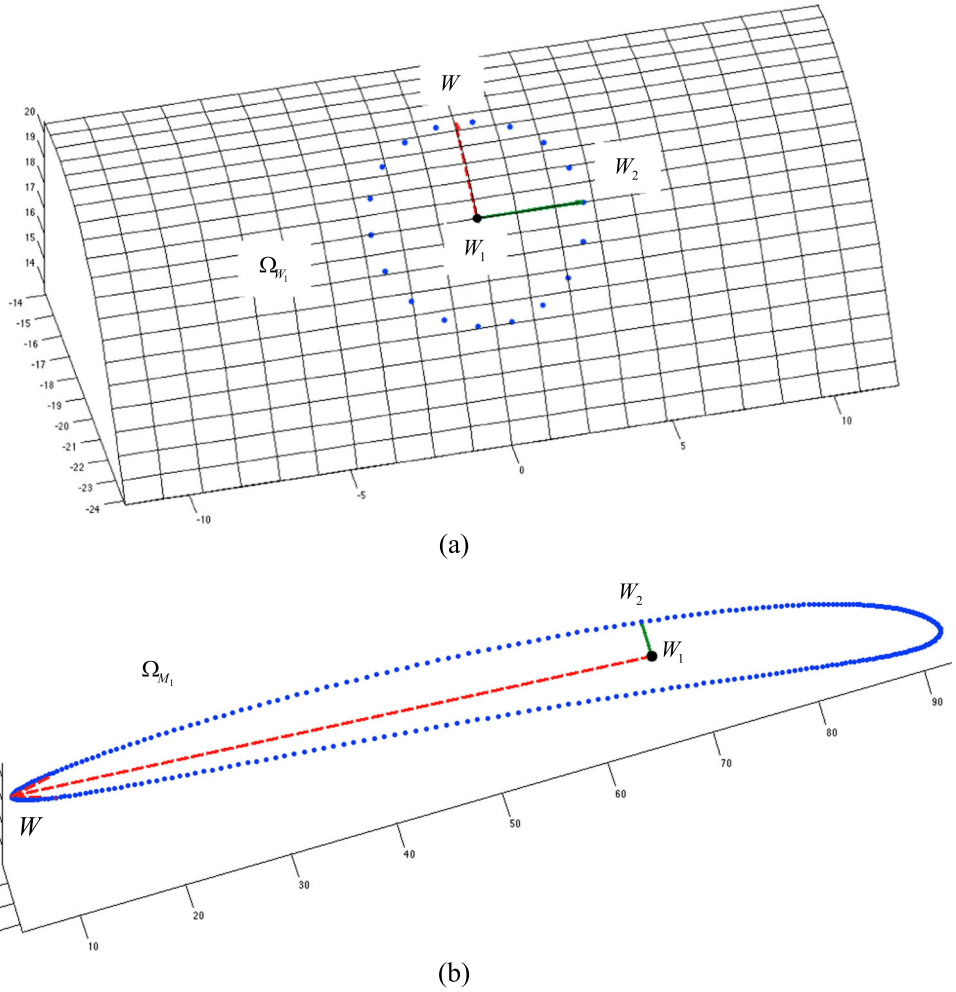

Fig. 6 Possible tool feed directions in the workpiece and the machine coordinates

controller performs the standard linear interpolation. The tool speed at a CC point along $\overrightarrow{W_1, W_2}$ is equal to the prescribed feed rate F. Note that these assumptions are not always realistic; however, one can replace the feed rate F by the magnitude of the actual velocity vector and use the evaluation given below without any further modifications.

The time required to move from W_1 to W is given by $t_1 = \frac{l_{1,M}(W)}{F}$. Consider the rotation angles (a_1,b_1) and (a,b) at W_1 and W, respectively. The required angular speed is given by $v_a = \frac{a_1-a}{t_1}$. Furthermore, if $v_a > v_{a,\max}$, where $v_{a,\max}$ is the maximum allowable rotational speed, we re-evaluate the material removal rate as follows: $R_M \equiv R_M(W) = \frac{l_1(W)w_1(W)}{t_{\text{new}}}$, where $t_{\text{new}} = \frac{a_1-a}{v_{a,\max}}$. A similar evaluation must be performed with regard to the second rotation angle b. The maximum allowed speed is evaluated from the cutting conditions and the material properties. The maximum cutting speed in the air is always given in the specifications of a 5-axis machine.

In order to reduce the machining time, we maximize the cost function $R_M(W)$ and generate the vector field of the optimal directions based on that particular but important criterion. For each (u_1, v_1) from the parametric domain K, we find $W_1 = S(u_1, v_1)$ and $W_2 = \text{argmax}_{W \in \Omega_{W_1}} R_M(W)$ (some advanced optimization methods can be applied to find W_2; however, this subject is beyond the scope of the paper).

Note that a variety of other cost functions related to the machine kinematics can be used to produce the required vector fields.

– *The total length of the tool path in the workpiece coordinates*. As noted, this criterion does not minimize the machining time. Although in many cases, it reduces the time but it is not as efficient as the proposed maximization of the material removal rate. The main advantage of this option is that it is machine independent. It is also independent with regard to the position and orientation of the workpiece on the table. The criterion is useful when the user is concerned about the tool wear (expensive tools for micro-milling or high-speed milling). The strategy to minimize the tool path in the workpiece coordinates is often based on maximization of the machining strip (see for instance [22]).

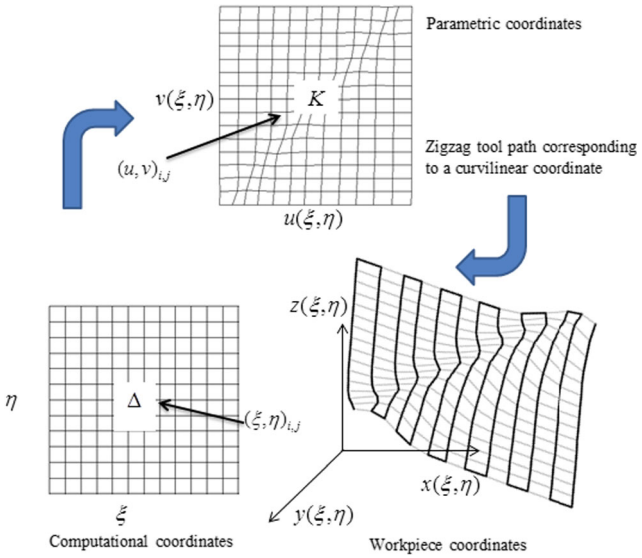

Fig. 7 Coordinate transformations and the curvilinear grids. Δ denotes the computational domain, K the parametric domain

- *The total length of the tool path in the machine coordinates*. This criterion can be also applied to minimize the machining time. It is often very efficient; however, it does not include the rotation angles. Therefore, the minimal tool path in the machine coordinates still does not mean a minimum time. More often than not, the direction of the minimal distance in the machine coordinates does not follow the direction of the maximum machining strip.
- *The kinematic error*. This optimization can be combined with the minimization of the machining time, for instance with the minimization of the material removal rate. In this paper, we apply a very basic approach based on additional CC points to keep the kinematic error within the prescribed tolerance. A more sophisticated version of such minimization can be found in [36].
- *The total angle variation*. This criterion can be applied to minimize the kinematic error which is invoked by the sharp rotations [37]. Minimizing the angle variation is less computationally expensive than minimizing the kinematic error explicitly ([26, 37]).

3 Grid generation

Let $S(u,v)\equiv(x(u,v),\ y(u,v),\ \ z\ (u,v))$ be the required part surface, where u and v are the parametric variables. We arrange the cutter location (CC) points $\{(u_{i,j},v_{i,j}),0\le i\le N_\xi,\ 0\le j\le N_\eta\}$ as a curvilinear grid in the parametric domain (u,v). Mathematically, it means that the CC points are the discrete analogy of a mapping from the computational region $\Delta=\{0\le\xi\le N_\xi,\ 0\le\eta\le N_\eta\}$ onto a parametric region defined in the parametric coordinates u and v. In other words, there exists a pair of functions $\{u(\xi,\eta),v(\xi,\eta)\}$ such that the rectangular grid $\{i,j\}$ being fed to $\{u(\xi,\eta),v(\xi,\eta)\}$ becomes $\{u_{i,j},\ v_{i,j}\}$ (see Fig. 7).

The required vector field $V(u,v)$ is partitioned into two vector fields $(\alpha(u,v),\beta(u,v))$ (the dual vector field) corresponding to the ξ and η directions as follows:

$$\alpha(u,v)=\begin{cases}V\ (u,v)\in\Omega_\xi,\\ 0,\ \ \text{otherwise},\end{cases},\beta(u,v)=\begin{cases}V\ (u,v)\in\Omega_\eta,\\ 0,\ \ \text{otherwise},\end{cases}$$

where Ω_ξ and Ω_η are prescribed subsets of the vector field $V(u,v)$ selected according to a certain criteria. For instance, if the vector field has two major directions (Fig. 8), d_ξ and d_η, the partition is performed as follows:

$$\alpha(u,v)=\begin{cases}\measuredangle\left(V,d_\xi\right)\approx 0\ \text{ or }\ \measuredangle\left(V,d_\xi\right)\approx\pi,\\ 0\ \ ,\qquad\text{otherwise}\ \ ,\end{cases}$$

$$\beta(u,v)=\begin{cases}\measuredangle\left(V,d_\eta\right)\approx 0\ \text{ or }\ \measuredangle\left(V,d_\eta\right)\approx\pi\\ 0\ \ ,\qquad\text{otherwise}\ \ .\end{cases}$$

In other words, the vectors $V(u,v)$ are included into the dual vector field $(\alpha(u,v),\ \beta(u,v))$ if they are almost parallel or almost antiparallel to d_ξ or d_η. Mathematically, it means that $\left|\left|\frac{(V,d)}{\|V\|\|d\|}\right|-1\right|\le\varepsilon_V$, where ε_V is the prescribed threshold.

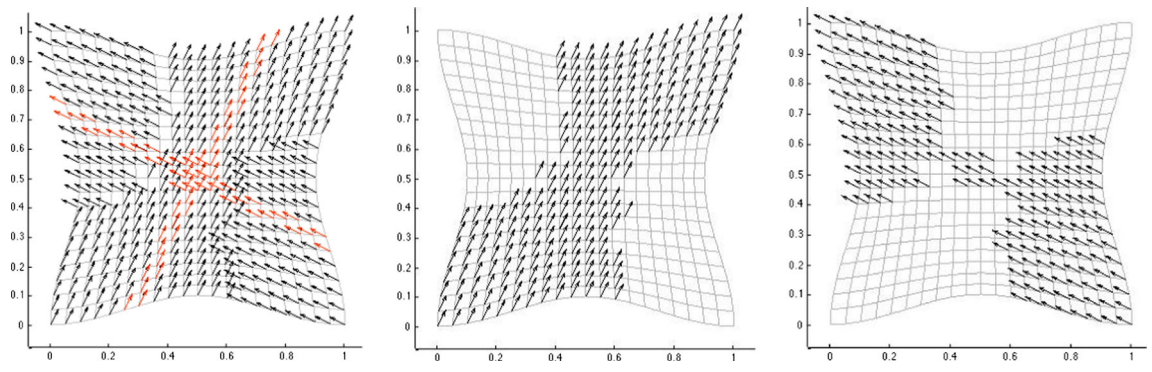

Fig. 8 Partition of the vector field $V(u,v)$ into $(\alpha(u,v),\beta(u,v))$

For vector fields with regular geometry, it is often sufficient to align only one family of grid curves. In this case, $\alpha(u,v)$ is a subset of $V(u,v)$, whereas $\beta(u, v)=0$. The vector field $(\alpha(u,v), \beta(u,v))$ can be further simplified. For instance, a point (u,v) can be considered "important" if the optimal direction substantially reduces the machining time, otherwise $\alpha(u,v)=\beta(u,v)=0$.

Furthermore, the curvilinear grid $\{u(\xi,\eta),v(\xi,\eta)\}$ is aligned with the dual vector field $(\alpha(u,v),\beta(u,v))$ using a modification of classical grid generation methods [38–40].

The smoothness of the grid is represented by a functional given by

$$F_S = \int\int u_\xi^2 + u_\eta^2 + v_\xi^2 + v_\eta^2 d\xi d\eta, \tag{1}$$

where subscripts denote the partial derivatives.

Note that F_s is a classical variational functional providing smoothness of the mapping $\{u(\xi,\eta),v(\xi,\eta)\}$ [39, 41]. Originally, the functional was applied to the tool path generation in [31]. The corresponding Euler equations for (1) are Laplacians able to offset the boundary due to their smoothing property. For example, if the boundary of the parametric region is a rectangle, functional (1) generates a rectangular grid corresponding to the conventional zigzag tool path. Furthermore, we show that a combination of the smoothness functional F_S and the vector field alignment generates the required curvilinear tool path.

For simplicity, consider alignment of the grid lines η=const with a vector field $\alpha(\xi,\eta)\equiv(\alpha_1(\xi,\eta),\alpha_2(\xi,\eta))$. The alignment is provided by a functional given by

$$F_A = \int\int \left(s_\xi \alpha'\right)^2 \mathrm{d}\xi \mathrm{d}\eta,$$

where $\alpha'(\xi,\eta)\equiv(\alpha_1',\alpha_2')=(-\alpha_2,\alpha_1)$ is the vector field perpendicular to $\alpha(\xi,\eta)$ and $s_\xi=(u_\xi,v_\xi)$ is the tangent to the grid line η=const. If s_ξ is parallel or antiparallel to α, then $F_A=0$. Following [39], the functionals F_S and F_A are combined linearly as follows: $\Phi=F_S+\lambda F_A$, where λ is the weighting coefficient.

The corresponding Euler equations are

$$\Phi_u - \Phi_{\xi,u_\xi} - \Phi_{\eta,u_\eta} = 0,$$
$$\Phi_v - \Phi_{\xi,v_\xi} - \Phi_{\eta,v_\eta} = 0.$$

Substitution $s_\xi\alpha'=u_\xi\alpha_1'+v_\xi\alpha_2'$ and differentiation yields

$$\begin{aligned} u_{\xi\xi} + u_{\eta\eta} + 2\lambda\left[\alpha_1'\left(\alpha_1' u_\xi + \alpha_2' v_\xi\right)\right]_\xi = 0, \\ v_{\xi\xi} + v_{\eta\eta} + 2\lambda\left[\alpha_2'\left(\alpha_1' u_\xi + \alpha_2' v_\xi\right)\right]_\xi = 0. \end{aligned} \tag{2}$$

Let us introduce a vector field $\beta(\xi,\eta)=(\beta_1(\xi,\eta),\beta_2(\xi,\eta))$ to be aligned with $s_\eta=(u_\eta,v_\eta)$. Equation (2) is then modified as follows

$$\begin{aligned} u_{\xi\xi} + u_{\eta\eta} + 2\lambda\left\{\left[\alpha_1'\left(\alpha_1' u_\xi + \alpha_2' v_\xi\right)\right]_\xi + \left[\beta_1'\left(\beta_1' u_\eta + \beta_2' v_\eta\right)\right]_\eta\right\} = 0, \\ v_{\xi\xi} + v_{\eta\eta} + 2\lambda\left\{\left[\alpha_2'\left(\alpha_1' u_\xi + \alpha_2' v_\xi\right)\right]_\xi + \left[\beta_2'\left(\beta_1' u_\eta + \beta_2' v_\eta\right)\right]_\eta\right\} = 0, \end{aligned} \tag{3}$$

where $\beta(\xi,\eta)\equiv\left(\beta_1',\beta_2'\right)=(-\beta_2,\beta_1)$.

Finally, we endow the proposed system of the elliptic partial differential equations with appropriate boundary conditions designed in such a way that the grid nodes slide along the boundary to adapt to the geometry of the grid lines inside the parametric region. Their positions are obtained iteratively by projecting the near-boundary nodes onto the boundary along the direction of the grid lines (see details in [38]).

The numerical solution of the system (3) is based on the discrete Laplacian, the central differences for the first derivatives and numerical iterations. The corresponding finite-difference equations are solved by the Newton method.

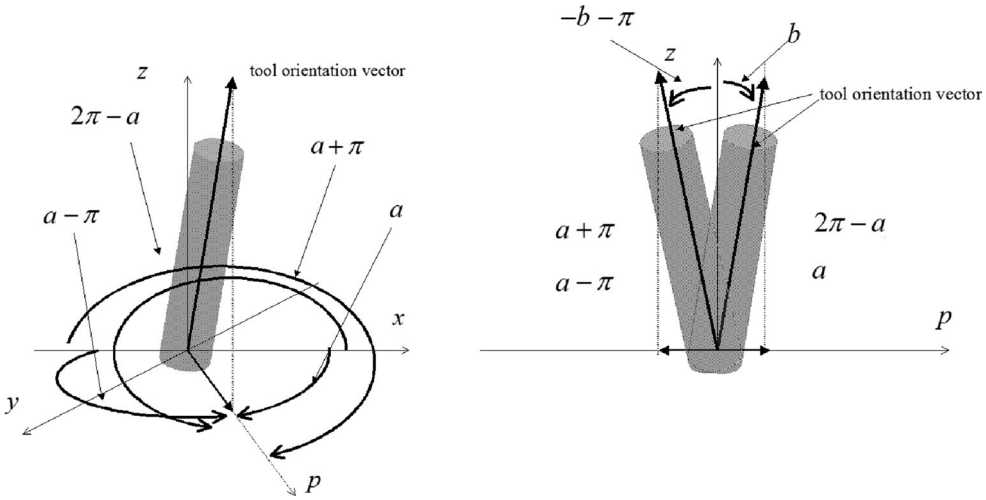

Fig. 9 Multiple solutions of the kinematics equations

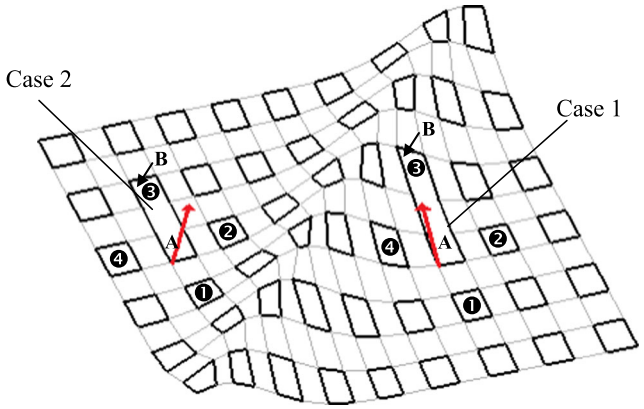

Fig. 10 BSFC: case 1 and case 2; *1*, *2*, *3*, and *4* denote R_{M_1}, R_{M_2}, R_{M_3}, and R_{M_4}, respectively

4 Kinematic errors and optimality measures

Let $W^D(s_p,s_{p+1},t)\in S(u,v)$ be a space curve between two tool positions W_p and W_{p+1} extracted from the machined surface $S(u,v)$, where $t\in[s_p,s_{p+1}]$ is a parametric coordinate along the curve. The kinematic error is the total distance between the desired trajectories $W^D_{p,p+1}(t)\equiv W^D(s_p,s_{p+1},t)$ and the actual trajectories $W_{p,p+1}(t)=W(s_p,s_{p+1},t)$ defined by

$$\varepsilon=\sum_p \operatorname{dist}\left(W^D_{p,p+1}(t),W_{p,p+1}(t)\right). \tag{4}$$

The actual trajectories are obtained by using the corresponding inverse kinematics transformations as follows. Consider a kinematics transformation $W=\Re(\Re,M)$ from the machine to the workpiece coordinates, where $W=(x,\ y,\ z)$, $M=(X,\ Y,\ Z)$ denote the workpiece and the machine coordinates and $\Re\equiv(a,b)$ the rotation angles. The procedure to derive the trajectories $W_{p,p+1}$ follows [37] (pages 40–42).

First, every W_p invoke the inverse transformation $M_p\equiv\Re^{-1}(\Re_p,W_p)$. Second, the rotation angles $\Re\equiv\Re(t)=(a(t),b(t))$ and the machine coordinates $M\equiv M(t)\equiv(x(t),y(t),z(t))$ are assumed to change linearly between the prescribed points s_p, s_{p+1} as follows:

$$M_{p,p+1}(t)=L_{p+1}(t)M_{p+1}+L_p(t)M_p,$$
$$\Re(t)=L_{p+1}(t)\Re_{p+1}+L_p(t)\Re_p,$$

where $L_{p+1}(t)=\frac{t-s_p}{s_{p+1}-s_p}$, $L_p(t)=\frac{s_{p+1}-t}{s_{p+1}-s_p}$, $s_p\le t\le s_{p+1}$.

Transforming M back to W for every t yields a trajectory of the tool tip in the workpiece coordinates given by

$$W_{p,p+1}(t)=\Re\left(\Re(t),M_{p,p+1}(t)\right)$$
$$=\Re\left(L_{p+1}(t)\Re_{p+1}+L_p(t)\Re_p\right\},L_{p+1}(t)M_{p+1}+L_p(t)M_p\big).$$

In order to represent the tool path in terms of the workpiece coordinates, we eliminate M_p and M_{p+1} by using the inverse transformation $M_p=\Re^{-1}(\Re_p,W_p)$.

Substituting, M_p and M_{p+1} yields $W_{p,p+1}(t)=\Re(L_{p+1}(t)\Re_{p+1}+L_p(t)\Re_p,L_{p+1}(t)\Re^{-1}(\Re_{p+1},W_{p+1})+L_p(t)\Re^{-1}(\Re_p,W_p))$.

Introduce a workpiece coordinate system O_1, a coordinate system of the first rotary part O_2, a coordinate system of the second rotary part O_3 and a coordinate system of the spindle O_4 (see Fig. 3).

As an example, consider a machine characterized by two rotary axes on the table (the so-called 0–2 machine, Fig. 3). It is not hard to demonstrate that $M\equiv\Re^{-1}\equiv\Re^{-1}\{\Re\}[W]=B[b](A[a](W+T_{12})+T_{23})+T_{34}-T_4$, where $T_4=(0,0,-L)$ and A and B are the corresponding rotation matrices. The coordinate transformation for other configurations such as 1–1 or 2–0 can be derived using a unified approach presented in [37].

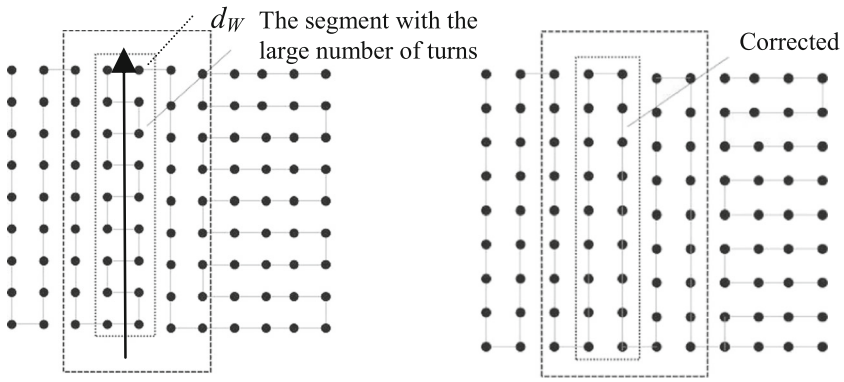

Fig. 11 Correcting the biased space-filling curve

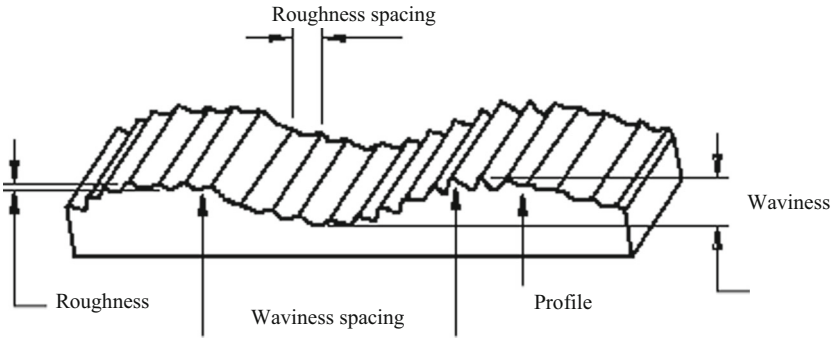

Fig. 12 Surface characteristics and terminology

If a is rotated so that the tool projection onto (x, y) is aligned with the positive y (Fig. 9) then

$$a = \begin{cases} \arctan\left(\frac{I_x}{I_y}\right) & \text{if } I_y > 0, \\ \arctan\left(\frac{I_x}{I_y}\right) - \pi & \text{if } I_y < 0, I_x \le 0, \\ \arctan\left(\frac{I_x}{I_y}\right) + \pi & \text{if } I_y < 0, I_x > 0, \end{cases}$$

$$b = \arccos I_z,$$

where (I_x, I_y, I_z) is the tool orientation vector.

It is well-known that the solution (a,b) of the above system is not unique. In order to reduce the kinematics error, we apply the shortest path optimization [29] with regard to the multiple solutions.

Furthermore, consider Eq. (4). Clearly, the error minimization procedure depends on the definition of the distance employed by (4). Some computationally simple choices are $\mathrm{dist}_2(W^D, W) = \| |W^D(t) - W(t)|_E \|_2$ $\mathrm{dist}_\infty(W^D, W) = \| |W^D(t) - W(t)|_E \|_\infty$, where $|\ |_E$ is the Euclidian distance and $W^D(t), W(t)$ are parameterized with regard to the pseudo time t. The above distances are differentiable and therefore are easy to be incorporated into standard minimization algorithms. They often produce good results when the compared curves are similar, arc-like segments.

Another good option is the rms distance based on a natural parameterization given by

$$\mathrm{dist}_N\left(W^D, W\right) = \sqrt{\int_0^1 \left|W^D(l_D(t)) - W(l(t))\right|^2 dt},$$

where $l_D(t)$ and $l(t)$ denote the corresponding arc-length parameterizations.

A serious drawback of dist_2, dist_∞, and dist_N is that they depend on the particular parameterization. Therefore, in this paper, we employ a parameterization-invariant Hausdorff distance given by

$$\mathrm{dist}_H\left(W^D, W\right) = \max\left\{ \max_{a \in W^D(t)} \min_{b \in W(t)} |a-b|_E, \max_{b \in W(t)} \min_{a \in W^D(t)} |a-b|_E \right\}.$$

Note that the tool trajectory is compared with the desired trajectory extracted *in some way* from the machined part. In engineering practice, the parts are defined by standard formats such STL, Standard for the Exchange of Product model data (STEP), Initial Graphic Exchange Specification (IGES), etc. For instance, the IGES represents curvilinear NURBS faces glued together along the boundary edges. Therefore, the method of extracting the trajectory should include the case of the multi-patch surfaces when the curve crosses the boundary or even several boundaries.

5 Biased space-filling curve

Although the generated curvilinear grid has been aligned with the prescribed vector field, the distance between the CC points has not been optimized with regard to the machining strip. Therefore, the grid is converted into a pair of continuous functions $u(\xi,\eta), v(\xi,\eta)$ using the bilinear interpolation. Next, we construct two iso-parametric paths in the ξ and η direction by calculating the largest tool path interval and using it as an offset as follows. The first tool track T_0 lies at the boundary

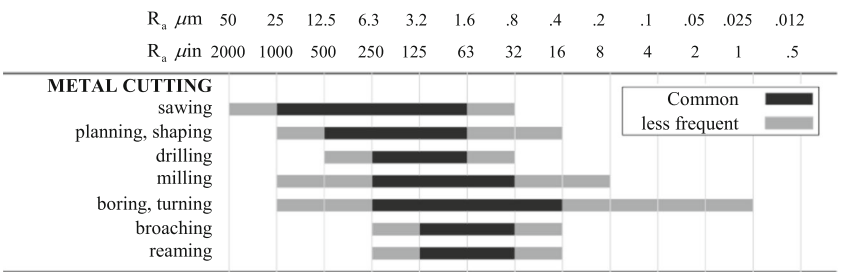

Fig. 13 Acceptable surface roughness

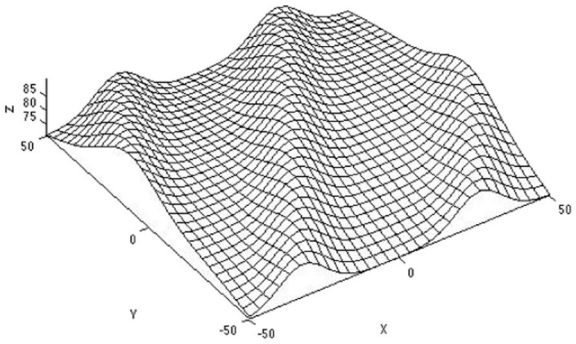

(a) The part surface

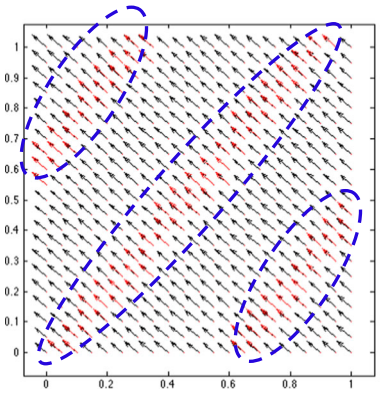

(b) vector field V_L

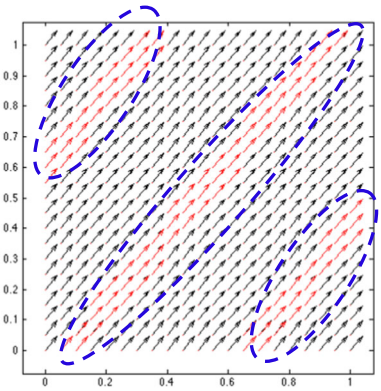

(c) vector field V_R

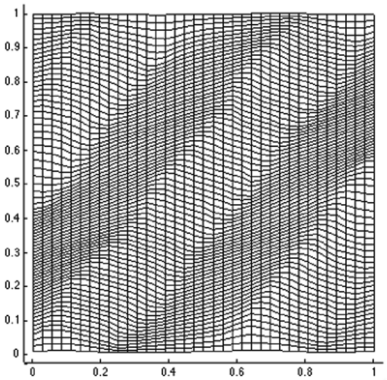

(d) grid G_L

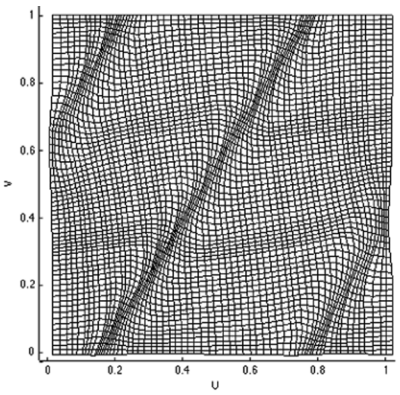

(e) grid G_R

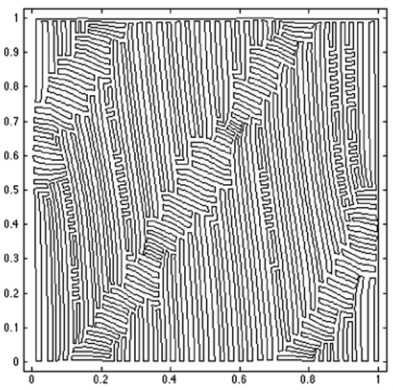

(f) SFC_L

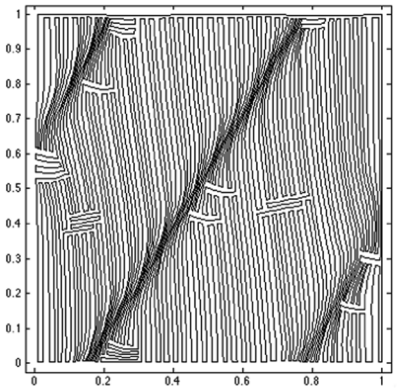

(g) SFC_R

Fig. 14 VFAP solution for surface 1

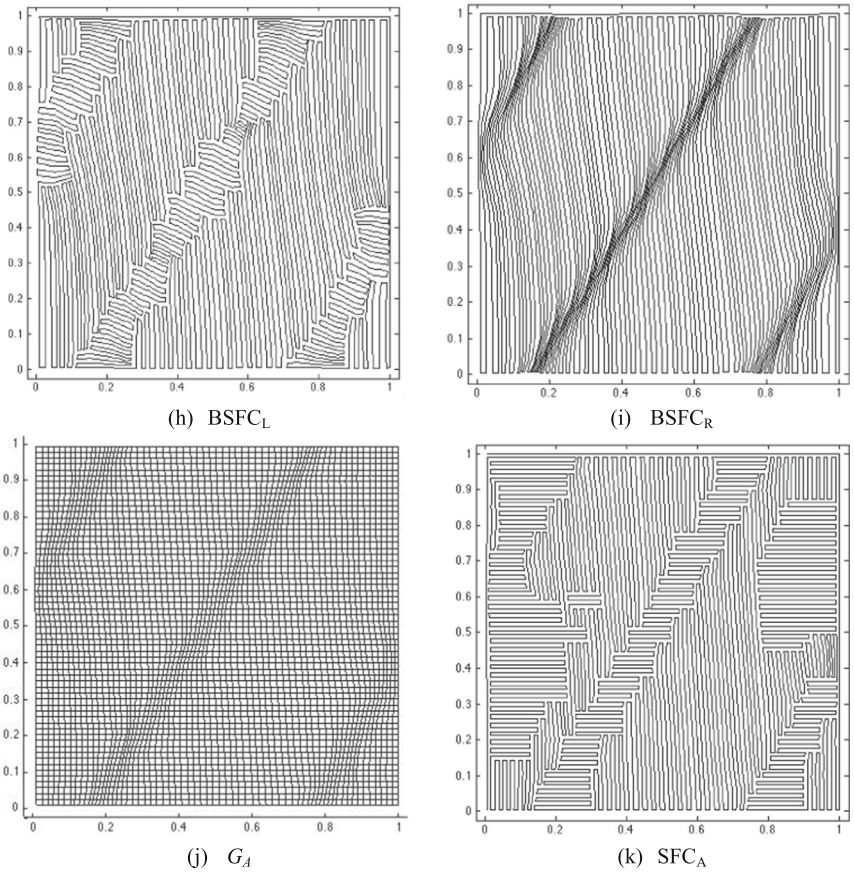

(h) $BSFC_L$ (i) $BSFC_R$

(j) G_A (k) SFC_A

Fig. 14 (continued)

of the parametric domain. Next, T_1 is a curve $\eta=\eta_1$ defined by $\{u(\xi,\eta_1),\ v(\xi,\eta_1)\}$ such that $\text{dist}_H(T_0,T_1)<w_{R,0}+w_{L,1}$, where $w_{L,0},w_{R,1}$ is the left and the right maximum allowed strip width. The next track is generated by $\{u(\xi,\eta_2),\ v(\xi,\eta_2)\}$ such that $\text{dist}_H(T_1,T_2)<w_{R,1}+w_{L,2}$. The two overlaying tool paths represented by the coordinate lines are characterized by the maximum possible machining strip between any pair of the adjacent tool tracks.

Next, the problem is simplified by thresholding the vector field as follows

$$I(\xi,\eta)=\begin{cases} V(\xi,\eta), & \text{if} \quad K_I > k', \\ (0,0), & \text{otherwise}, \end{cases} \tag{5}$$

where k' is the prescribed threshold and K_I is the measure of importance of the particular point. We consider two measures, $\max|K|$, where K is the curvature of the surface and $\max R_M - \min R_M$. The first measure is the basic characteristic of the surface implying that if the curvature of the surface is high, the feed direction is important. The second measure tells you that if the difference between the maximum and the minimum material removal rate at the particular point is large, the feed direction is important. Equation (4) defines "important points" where $I(u,v)\neq 0$ and "unimportant points" where $I(u,v)=0$.

Furthermore, the rectangular grid in (ξ,η) is regarded as an undirected graph G, where each two adjacent cells are connected by an edge. The cells are then connected by the biased adaptive space-filling curve (BSFC) using the following procedure.

Consider an important cell A.

Case 1. The grid is well aligned with the vector field. In this case, A can be connected with one of the neighboring cells B such that $\overrightarrow{AB}$ is almost parallel or almost antiparallel to the direction of the corresponding vector field $V(\xi,\eta)$ (see Fig. 10).

Case 2. The grid is not well aligned with the vector field. In this case, none of the directions $\overrightarrow{AB}$ is close to $V(\xi,\eta)$. Therefore, we evaluate the material removal rate R_{M_1}, R_{M_2}, R_{M_3}, and R_{M_4} in the four possible directions and connect in the direction of the $\max_i R_{M_i}$ (as shown in Fig. 10).

Finally, if cell A is unimportant, we connect it with one of the four neighboring cells randomly. Within this framework, it is often practical to use the "tracing bug" techniques designed to avoid frequent turns. In this case, the unimportant cell is

connected to the next cell following the direction of the tracing bug from the preceding step.

Finally, the BSFC is a modification of the adaptive SFC proposed in [42]. The advantage of BSFC is the reduction of the machining time by following a set of the prescribed directions at the important points. Furthermore, large kinematic errors appear when the tool feed vector abruptly changes direction. Therefore, the BSFC decreases the kinematic error by reducing frequent sharp turns using the following correction. For each point, we calculate the number of the preceding consecutive turns. The segments with a large number of turns will be marked and the vector field $V(\xi,\eta)$ at each point of this segment will be adjusted as follows: $V(\xi,\eta)=d_W(\xi,\eta)$, where $d_W(\xi,\eta)$ denotes the "principal direction" in a window around a segment as shown in Fig. 11. The procedure can be considered as a high frequency filter.

6 Quality of the machined surface

We measure the quality of the machined surface in terms of its roughness and waviness. Roughness represents micro peaks and valleys of the surface produced by the tool while waviness is often attributed to the vibrations. Waviness often increases when the milling machine operations involve large and sharp periodic rotations. Considering the surface as a 2D signal, the roughness is associated with high frequencies of the signal and the waviness with medium frequencies (Fig. 12).

We measure the roughness by one of the most commonly used methods called the stylus contact profiling [43]. The surface profile obtained by a high-resolution probe is post processed by the Gaussian filter [44]. The surface roughness is given by $R_a = \frac{1}{N}\sum_{i=1}^{N}|y_i|$, where y_i is the height of the profile

Table 1 VFAP vs. conventional tool paths. Surface 1

Tool radius 4 mm			Tool path generation method		Scallop height (mm)		
					0.25	0.1	0.05
Performance	Tool path length (mm)		Master CAM		34,698.0	75,392.0	144,098.0
			UG	HS	30,713.0	74,354.0	148,130.0
				FP	6707.8	10,833.0	15,280.0
			ISO Zigzag		6371.9	10,187	14,535
			G_A	SFC_L	4417.9	6605.3	9367.5
			$VFAP_L$		4473.3	6176.1	8610.3
			$VFAP_R$		4724.1	7117.0	9947.0
	Machining time	MAHO 600 E	UG	HS	3:24:33.8	8:18:32.6	16:37:30.3
				FP	0:39:34.1	1:05:15.8	1:33:52.2
			ISO Zigzag		0:28:01.0	0:44:58.0	1:04:21.0
			G_A	SFC_L	0:27:15.3	0:42:36.5	0:59:32.2
			$VFAP_L$		0:27:13.2	0:42:10.7	0:58:18.5
			$VFAP_R$		0:18:14.2	0:28:03.4	0:40:04.2
		Haas VF-2TR	UG	HS	6:15:24.6	15:07:51.0	30:07:46.4
				FP	0:39:35.6	2:13:45.3	3:10:43.1
			ISO Zigzag		0:45:08.0	1:12:41.0	1:43:41.0
			G_A	SFC_L	0:44:34.2	1:09:20.5	1:37:29.2
			$VFAP_L$		0:43:57.9	1:08:40.3	1:35:52.4
			$VFAP_R$		0:33:52.7	0:52:47.5	1:14:28.2
Advantage rel. to ISO	Tool path length (mm)		G_A	SFC_L	30.7 %	35.2 %	35.6 %
			$VFAP_L$		29.8 %	39.4 %	40.8 %
			$VFAP_R$		25.9 %	30.1 %	31.6 %
	Machining Time	MAHO 600 E	G_A	SFC_L	2.7 %	5.2 %	7.5 %
			$VFAP_L$		2.8 %	6.2 %	9.4 %
			$VFAP_R$		34.9 %	37.6 %	37.7 %
		Haas VF-2TR	G_A	SFC_L	1.2 %	4.6 %	6.0 %
			$VFAP_L$		2.6 %	5.5 %	7.5 %
			$VFAP_R$		24.9 %	27.4 %	28.2 %

relative to a mean Gaussian curve and N is the total number of the measurement points. Furthermore, the Gaussian filter allows us to evaluate waviness by subtracting the roughness profile from the raw profile.

We measured 20 sample profiles with the standard cutoff of 0.8 mm [44]. The average value was compared with the roughness and waviness produced by the conventional method. The roughness of the machined surfaces was within the acceptable range for surface milling operations, that is, between 0.2 and 25 μm [45] (see Fig. 13).

7 Numerical examples and cutting experiments

In this section, the proposed VFAP-BSFC method is compared with the iso-parametric zigzags tool path (ISO) for three convex-concave parts. We also test the method against MasterCAM X5, "Follow Periphery" (UG-FP), "Helical or Spiral" (UG-HS) options of Unigraphics NX9 and the adaptive curvilinear SFC [42]. The test surfaces were initialized in the MasterCAM environment using a parametric representation. Next, the surfaces were exported into the STEP or IGES formats and imported into the UG.

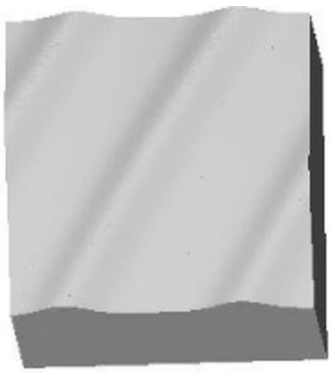

(a) conventional zigzag, virtual cut

(b) conventional ISO zigzag, actual cut,
tool path length = 14535.0 mm, time = 1:43:41 hrs

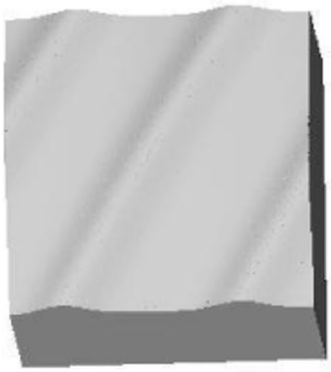

(c) $VFAP_L$, virtual cut

(d) $VFAP_L$, actual cut,
tool path length = 8610.3 mm (**advantage 40.8%**),
time = 1:35:52 hrs (**advantage 7.5%**)

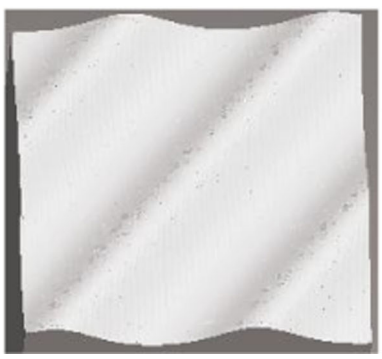

(e) $VFAP_R$, virtual cut

(f) $VFAP_R$, actual cut,
tool path length = 9947.0 mm (**advantage 31.6%**),
time = 1:14:28 hrs (**advantage 28.2%**)

Fig. 15 Test surface 1. Virtual and real machining

Table 2 Kinematic error VFAP vs. conventional tool paths. Surface 1

	Tool path generation method		Hausdorff distance between the actual and required trajectory								
			h=0.25			h=0.10			h=0.05		
			#CC	Ave	Std	#CC	Ave	Std	#CC	Ave	Std
MAHO 600 E	UG	HS	5557	0.055	0.059	32,351	0.033	0.026	120,327	0.020	0.013
		FP	1139	0.047	0.057	7329	0.029	0.025	14,542	0.018	0.013
	ISO Zigzag		4574	0.075	0.057	9339	0.043	0.023	17,940	0.024	0.011
	G_A	SFC_L	3390	0.106	0.059	7577	0.045	0.024	14,932	0.023	0.012
	$VFAP_L$		3552	0.097	0.059	7413	0.043	0.023	14,601	0.022	0.012
	$VFAP_R$		2622	0.085	0.058	5689	0.042	0.023	11,526	0.021	0.012
Haas VF-2TR	UG	HS	8649	0.066	0.063	48,163	0.037	0.026	169,196	0.022	0.012
		FP	1675	0.057	0.060	8154	0.034	0.026	18,810	0.034	0.027
	ISO Zigzag		4677	0.087	0.058	10,205	0.044	0.022	19,455	0.025	0.011
	G_A	SFC_L	3510	0.108	0.060	8178	0.045	0.023	16,603	0.023	0.011
	$VFAP_L$		3652	0.104	0.061	8159	0.045	0.023	16,373	0.023	0.011
	$VFAP_R$		2805	0.095	0.060	6323	0.043	0.022	12,910	0.022	0.011

The conventional methods and VFAP have been applied with an appropriate setup optimization [14]. The accuracy of the machining has been evaluated in terms of the kinematic error, roughness, and waviness. All surfaces have been machined by the flat-end tool.

We also test the proposed cost function against minimization based merely on the length of the tool path. In this case, the vector field is generated along the direction of the maximum machining strip and the BSFC is based on the length of the tool path. The corresponding cost function is evaluated by replacing the material removal rates with the length of the tool path between the corresponding nodes. We will indicate the material removal rate and the tool path length versions of the optimization by subscripts R and L respectively, for instance $VFAP_R$ and $VFAP_L$.

7.1 Example 1. A concave–convex surface with multiple peaks. Rough cut

The example demonstrates the efficiency the VFAP with the reference to the traditional iso-parametric path (ISO), an automatic tool path generation procedure of MasterCAM X5 as well as the algorithms UG-FP and UG-HS. We also test $VFAP_L$ against $VFAP_R$ and against the adaptive SFC based on the kinematic error proposed in [42].

Consider a surface in Fig. 14a given by

$$x(u,v) = 100u{-}50,\ \ y(u,v) = 100v{-}50,$$
$$z(u,v) = 11.6e^{-30(v-1.7u+0.3)^2} + 11.6e^{-30(v-1.7u+1.3)^2} + 11.6e^{-30(1.7u-v+0.6)^2} {-} 33.3v(v{-}1) + 70.$$

The corresponding vector fields V_L and V_R are shown in Figs. 14b, c, respectively, where the dashed lines indicate the important points. The curvilinear grids G_L and G_R adapted to the prescribed vector fields are shown in Figs. 14d, e. SFC_L and SFC_R are displayed in Fig. 14f, g, whereas the proposed $BSFC_L$ and $BSFC_R$ are shown in Figs. 14h, i. Additionally, we generated a curvilinear grid G_A and the corresponding adaptive SFC_A [42] shown in Figs. 14j, k. The grid and the SFC_A tool path have been constructed using the minimization of the kinematic error [42]. The surface was machined virtually by

Table 3 Roughness and Waviness of VFAP vs. the conventional tool paths. Surface 1

Roughness R_α (μm)			Standard deviation			Waviness (μm)			Standard deviation		
ISO zigzag	$VFAP_L$	$VFAP_R$	ISO zigzag	$VFAP_L$	$VFAP_R$	ISO zigzag	$VFAP_L$	$VFAP_R$	ISO zigzag	$VFAP_L$	$VFAP_R$
6.7	6.2	6.1	9.1	8.5	3.7	26.9	26.9	13.7	8.1	7.9	4.7

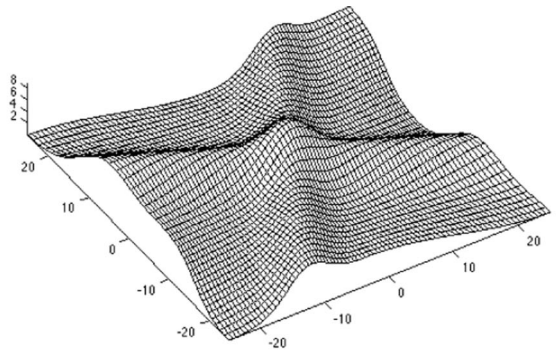

(a) Test surface 2

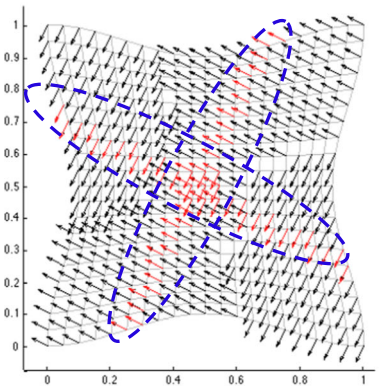

(b) vector field V_L

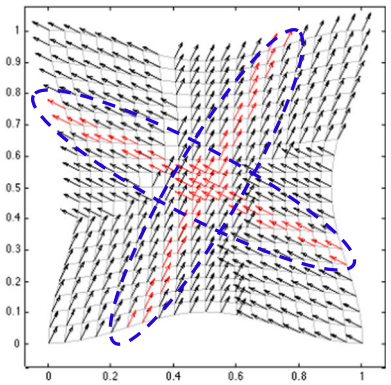

(c) vector field V_R

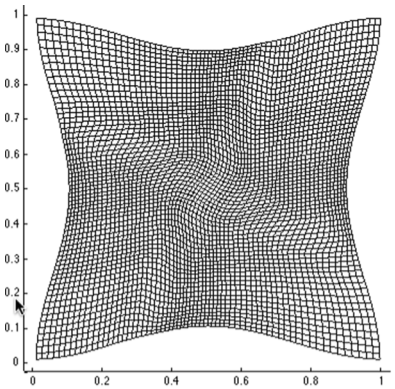

(d) grid G_L

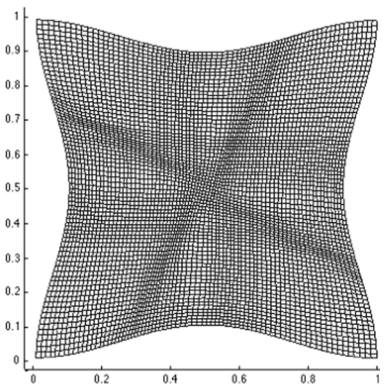

(e) grid G_R

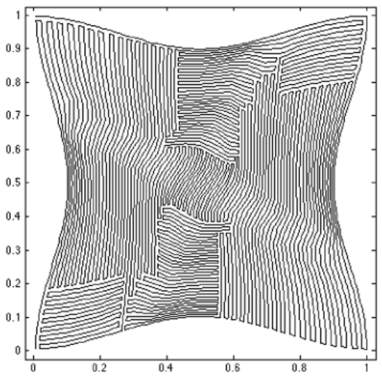

(f) $BSFC_L$

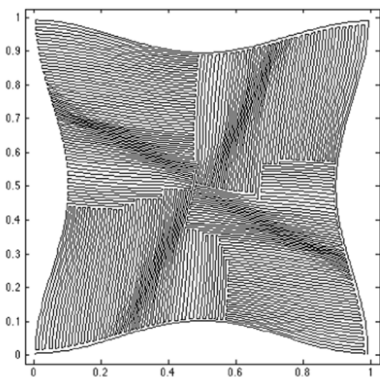

(g) $BSFC_R$

Fig. 16 VFAP solution for surface 2

Vericut 7.0 and on the 5-axis machine Haas VF-2TR by a flat-end tool with the radius 4 mm.

The results obtained by the VFAP technology compared with the conventional ISO tool path, MasterCAM X5, UG-FP, UG-HS, and the adaptive SFC_A are given in Table 1. The improvement is defined as $\frac{\text{before}-\text{after}}{\text{before}}100$. The machining depends on the configuration of the machine, position of the workpiece, and the prescribed scallop height; however, VFAP always provides an improvement. Furthermore, $VFAP_R$ designed to reduce the machining time provides 37 and 28 % improvement of the machining time for the MAHO 600 E and Haas VF-2TR, respectively, whereas $VFAP_L$ generates 40 % improvement in terms of the tool path length. This is considerable progress considering hundreds or even thousands of hours typically spent for machining complicated industrial parts.

Figure 15 show the surface obtained by the ISO tool path vs. surfaces machined using the proposed method. Table 1 displays the advantages of the method. For instance, the maximum allowed scallop of 0.05 mm requires 1 h and 4 min and 1 h and 43 min for a non-optimal tool path on MAHO 600 E and Haas VF-2TR, whereas with the optimization, the machining requires 40 min and 1 h and 14 min, respectively. Clearly, it is an impressive advantage for such a small workpiece of 100×100 mm.

Observe an overwhelming advantage over the tool path generated by MasterCAM X5. For h=0.25, 0.1, and 0.05 mm, the tool path length has been reduced by factors of 4, 10, and 14, respectively. Furthermore, the UG tool path is considerably better than that generated by MasterCAM and the proposed method outperforms UG as well. For instance, compared to UG-FP, the tool path has been reduced by 34, 43, and 43.5 % for h=0.25, 0.1, and 0.05, respectively.

There is a clear advantage in the machining time as well. For example, on MAHO 600 E for h=0.25 the $VFAP_R$ requires 40 min vs. 1 h and 33 min using UG-FP and 16 h and 37 min(!) using UG-HS(see a detailed comparison in Table 1).

Finally, cutting large complex industrial parts with high accuracy employs tens or hundreds of thousands, and even millions of CC points and hundreds of hours. Therefore, the improvement in the tool path length and in the machining time is significantly saving long hours of machining and reducing wear on the tool.

Table 2 displays the kinematic error. The constraint imposed on the scallop height h is used as an upper limit for the allowable kinematic error. If the kinematic error between

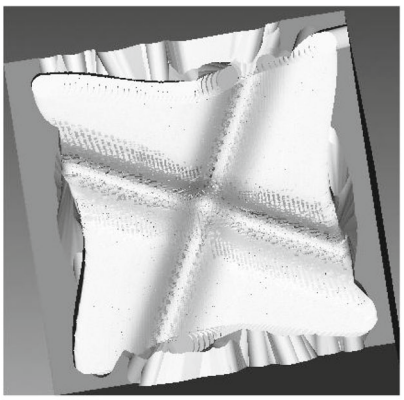

(a) conventional ISO zigzag tool path length= 5644.3 mm, time = 1:15:03 hrs

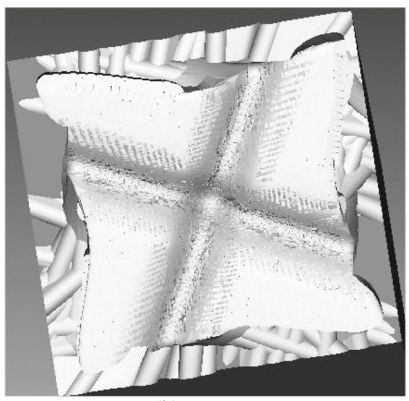

(b) $VFAP_L$,
tool path length = 4323.5 mm (**advantage 23.4%**),
time = 1:13:12 hrs (**advantage 2.5%**)

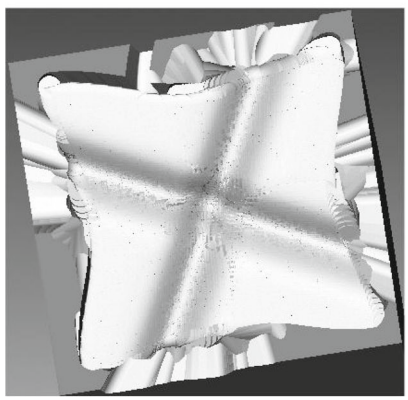

(c) $VFAP_R$,
tool path length = 5323.8 mm (**advantage 5.7%**) ,
time = 0:56:26 hrs (**advantage 24.8%**)

Fig. 17 Example 2. Machined surfaces

two CC points exceeds h, an additional CC point is inserted until $\max(\varepsilon) \le h$. Next, we evaluate the average error given by $\varepsilon' = \frac{\sum_{k=0}^{m-1} \varepsilon_k}{m}$, where m is the number of trajectories. If $\varepsilon' << h$, the surface is close to the required surface not only in the sense of the maximum Hausdorff distance, but in the sense of the average Hausdorff distance as well. This indicates a good quality of the surface.

Clearly, the average error is a small fraction of the required accuracy h. As a matter of fact, the difference between the results is in the range of 0.02 for h=0.25, 0.01 for h=0.1, and 0.001 for h=0.05. For the majority of the modern milling machines, this difference still lies outside the range of machining accuracy. Therefore, the proposed method provides a tangible increase in terms of the length of the tool path and the machining time while maintaining the same accuracy. Table 2 demonstrates that the method substantially reduces the number of required CC points for high-accuracy milling (h=0.1 and h=0.01). Note that the decrease in the number of the CC points is, in particular, important for high-speed milling when the programmed feed rate can exceed the sampling speed of the controller.

Table 3 displays the average roughness and waviness of the machined surface. Roughness of $VFAP_L$,$VFAP_R$, and ISO zigzag is 6.1, 6.2, and 6.7 μm, respectively, whereas the waviness of $VFAP_L$ is about 14 μm and $VFAP_R$ and ISO zigzag is about 27 μm for both cases. Therefore, the surface generated by the proposed method is characterized by a slightly better roughness and waviness relative to the conventional ISO path while outperforming the conventional zigzag in terms of the cutting time and the length of the tool path. Finally, the measured roughness complies with the standard industrial requirements for the quality of the surface milling (see Fig. 13).

7.2 Example 2. A peak-crossing surface

Analyzing surface 1 above characterized by the parallel diagonal peaks, one may arrive at the following question. “Can we rotate the standard zigzag path so that the cut is performed along the optimal direction?” Unfortunately, it is not always possible. Consider a surface in Fig. 16a given by

$$x(u,v) = 50u - 25,\ \ y(u,v) = 50v - 25,\ \ z(u,v) = 4.5\left(e^{-30(v-2u+0.5)^2} + e^{-30(u+2v-1.5)^2}\right).$$

Table 4 VFAP vs. conventional tool paths. Surface 2

Tool radius 2 mm			Tool path generation method		Scallop height(mm)		
					0.25	0.1	0.05
Performance	Tool path length (mm)		Master CAM		6325.5	13,760.0	23,294.4
			UG	HS	6555.2	15,595.5	33,865.5
				FP	3283.6	5138.9	7260.3
			ISO zigzag		2591.4	4021.7	5644.3
			$VFAP_L$		2036.1	3125.0	4323.5
			$VFAP_R$		2483.9	3807.4	5323.8
	Machining Time	MAHO 600 E	UG	HS	0:34:55.3	1:22:50.4	3:02:12.2
				FP	0:20:08.2	0:32:17.8	0:46:07.8
			ISO zigzag		0:08:05.2	0:12:40.4	0:17:51.8
			$VFAP_L$		0:07:53.8	0:12:18.6	0:17:10.2
			$VFAP_R$		0:06:29.9	0:09:55.3	0:13:47.7
		Haas VF-2TR	UG	HS	2:59:36.0	7:10:23.0	14:54:48.8
				FP	1:27:46.9	2:18:47.6	3:16:01.8
			ISO zigzag		0:33:48.7	0:53:10.3	1:15:03.7
			$VFAP_L$		0:34:21.1	0:52:03.5	1:13:12.6
			$VFAP_R$		0:26:42.5	0:41:55.5	0:56:26.1
Advantage rel. to ISO	Tool path length (mm)		$VFAP_L$		21.4 %	22.3 %	23.4 %
			$VFAP_R$		4.1 %	5.3 %	5.7 %
	Machining Time	MAHO 600 E	$VFAP_L$		2.3 %	2.9 %	3.9 %
			$VFAP_R$		19.6 %	21.7 %	22.8 %
		Haas VF-2TR	$VFAP_L$		−1.6 %	2.1 %	2.5 %
			$VFAP_R$		21.0 %	21.2 %	24.8 %

Table 5 Kinematic error. VFAP vs. conventional tool paths. Surface 2

	Tool path generation method		Hausdorff distance								
			h=0.25			h=0.10			h=0.05		
			#CC	Ave	Std	#CC	Ave	Std	#CC	Ave	Std
MAHO 600 E	UG	HS	2130	0.043	0.056	9940	0.026	0.025	37,174	0.018	0.012
		FP	1732	0.055	0.061	5973	0.032	0.027	12,115	0.019	0.013
	ISO zigzag		4584	0.030	0.046	7834	0.021	0.022	12,306	0.015	0.012
	$VFAP_L$		2330	0.057	0.061	5678	0.030	0.026	11,922	0.016	0.013
	$VFAP_R$		2436	0.035	0.041	5998	0.013	0.014	11,957	0.007	0.007
Haas VF-2TR	UG	HS	7268	0.085	0.064	34,395	0.041	0.025	113,968	0.024	0.011
		FP	4192	0.085	0.068	12,240	0.041	0.026	27,106	0.022	0.012
	ISO zigzag		5164	0.059	0.065	9966	0.032	0.025	17,349	0.020	0.012
	$VFAP_L$		3378	0.095	0.069	8610	0.041	0.025	18,536	0.021	0.012
	$VFAP_R$		2789	0.064	0.061	6709	0.023	0.023	13,444	0.012	0.012

The corresponding vector fields V_L and V_R are shown in Figs. 16b, c. The diagonal clusters of important points are indicated by the dashed lines.

Clearly, the abovementioned re-orientation cannot provide the required alignment. Besides, the surface is defined on a curvilinear rectangle which creates additional problems for a conventional tool path generation. Therefore, the curvilinear grids G_L and G_R in Fig. 16d, e are generated using the dual vector field technology (see Fig. 8). The corresponding $BSFC_L$ and $BSFC_R$ are shown in Fig. 16f, g. The virtual cuts performed with the 2-mm flat-end tool radius and the 0.25-mm maximum scallop heights are shown in Fig. 17a–c for ISO, $VFAP_L$, and $VFAP_R$, respectively.

Table 4 demonstrates advantages of the proposed method over ISO, MasterCAM X5, UG-FP, and UG-HS. The proposed method outperforms the above algorithms for every prescribed scallop height. For instance, for h=0.25 mm $VFAP_L$ tool path is 5.3 times shorter than that generated by MasterCAM, 23 % shorter than ISO, 7.8 times shorter than UG-HS, and 40 % shorter than UG-FP.

There is a clear advantage in the machining time as well. For instance, MAHO 600 E for h=0.05 the $VFAP_R$ requires 13 vs. 46 min using UG-FP and 3 h and 2 min using UG-HS(see the full evaluation in Table 4).

Table 5 shows the accuracy of the proposed method in terms of the kinematic error. The error behaves similarly to Example 1 with negligible deviations from the prescribed accuracy. Still, the orientation may help. As a matter of fact, a complicated surface may require a combination of orientation and the proposed BSFC. However, as long as there is at least one non-linear or even diagonal cluster of important points, there always will be benefits provided by the VFAP technology.

Finally, as opposed to Example 1 where only one family of the grid curves was adapted to the required vector field (see Eq. (2)), Example 2 shows the efficiency of the method applied with the dual vector fields.

7.3 Example 3. A semi-oval ridge (composite grid). Rough and fine cut

A surface in Fig. 18a is characterized by a ridge nearby the boundary. We adopted this shape from the dental micro-milling where the elevated part represents the ridges of a

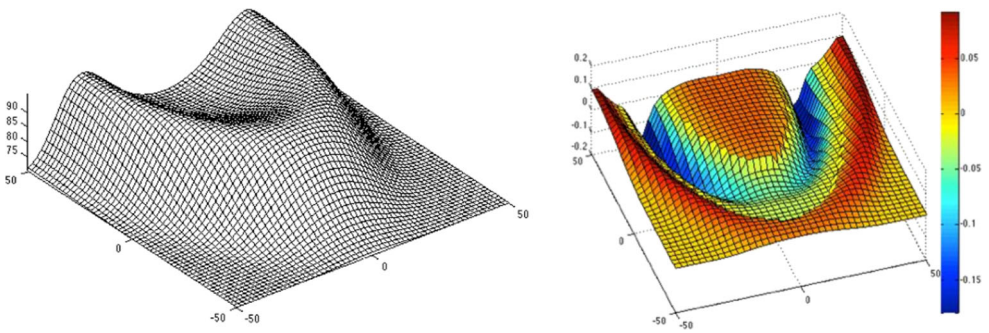

Fig. 18 Test surface 3 and its curvature

(a) Test Surface 3 (b) The curvature

dental crown or implant [46]. The VFAP for such surfaces can be combined with a decomposition of the parametric region and generation of a curvilinear grid in each subregion. Figure 18b shows that the most important region is a semi-circular ridge nearby the boundary characterized by the high curvature

We model a situation when the user needs a minimal tool path for the rough cut to reduce the tool wear and the minimal time for the fine cut. The proposed tool path generation method allows for these strategies. The rough machining is performed along the direction of the highest curvature in order to maximize the machining strip, that is, $VFAP_L$. This

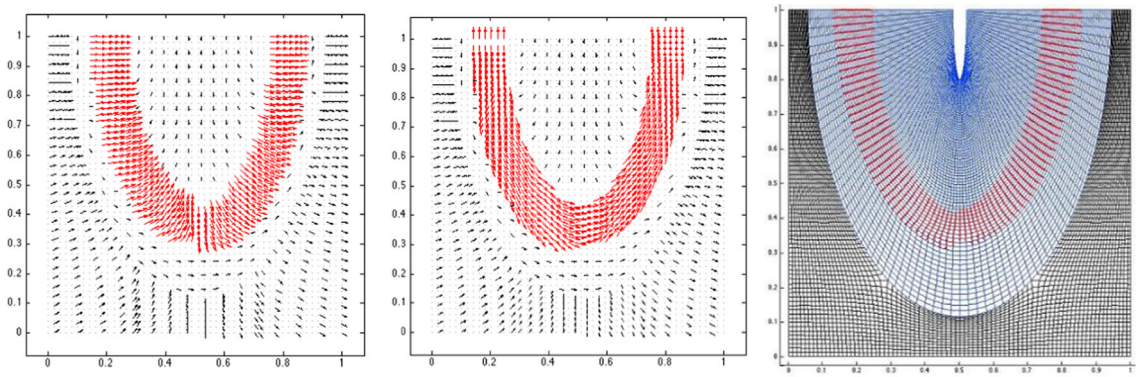

vector field V_L vector field V_R curvilinear grid

(a) Vector fields V_L and V_R and the composed curvilinear grid G_{LR}

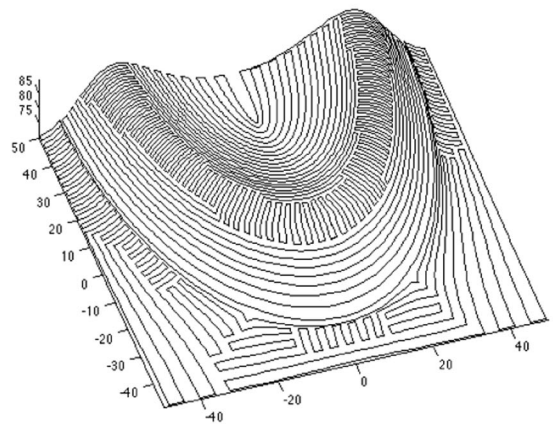

(b) $BSFC_L$, rough cut

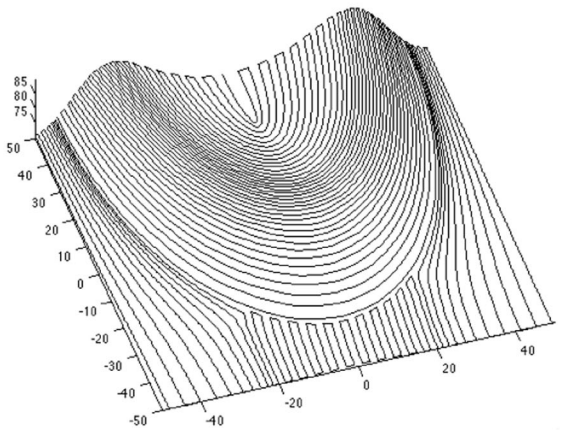

(c) $BSFC_R$, rough cut

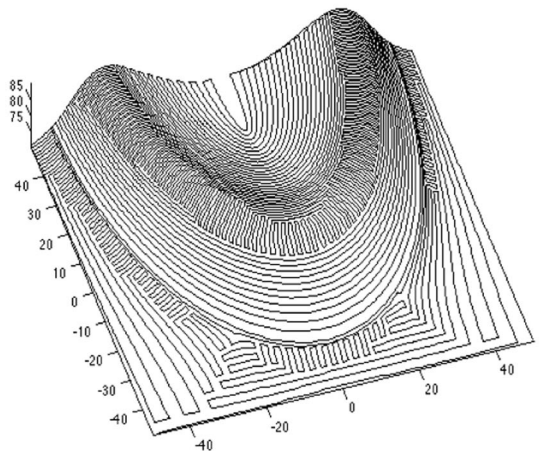

(d) $BSFC_L$, fine cut

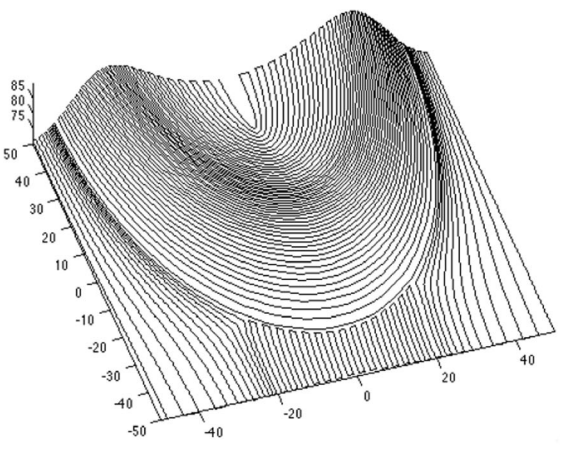

(e) $BSFC_R$, fine cut

Fig. 19 VFAP solution for surface 3

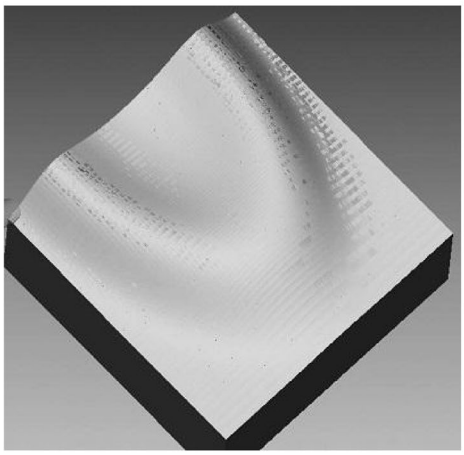

(a) Virtual machining ISO zigzag, rough cut

(b) Real machining, zigzag ISO, rough cut
tool path length= 12034.0 mm, time = 2:01:03 hrs

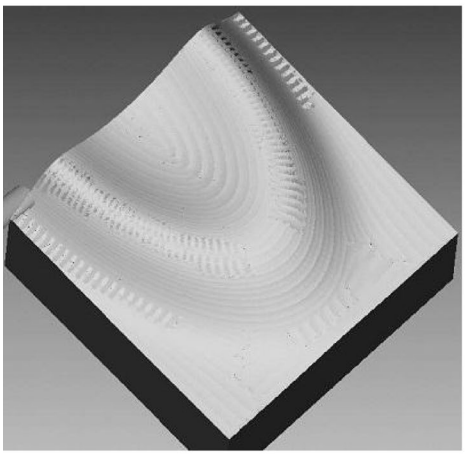

(c) Virtual machining $VFAP_L$, rough cut

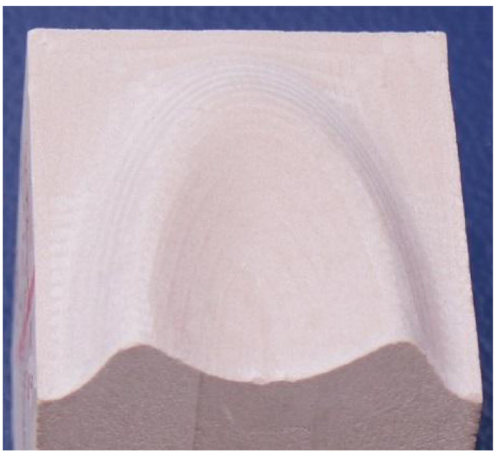

(d) Real machining $VFAP_L$, rough cut,
tool path length = 9545.7 mm (**advantage 20.7%**),
time = 1:55:52 hrs (**advantage 4.3%**)

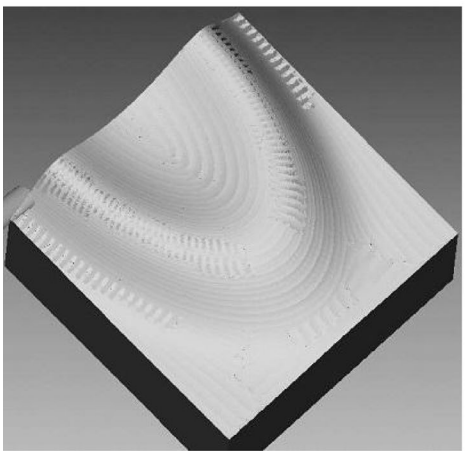

(e) Virtual machining $VFAP_R$, rough cut

(f) Real machining $VFAP_R$, rough cut,
tool path length = 10075.0 mm (**advantage 16.3%**),
time = 0:33:36 hrs (**advantage 72.2%**)

Fig. 20 VFAP vs. the ISO zigzag

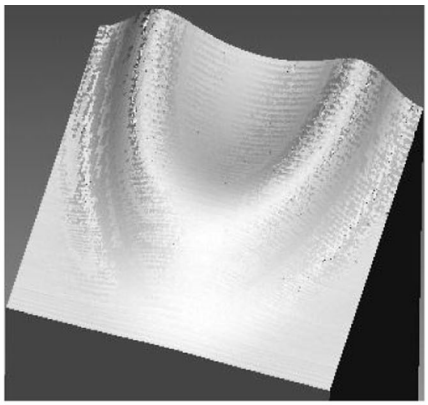

(g) Virtual conventional cut, fine cut

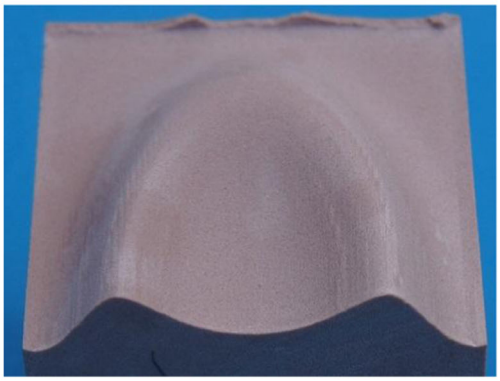

(h) Real machining, zigzag ISO, fine cut
tool path length= 26305.0 mm (**advantage 20.9%**),
time = 4:27:22 hrs (**advantage 7.1%**)

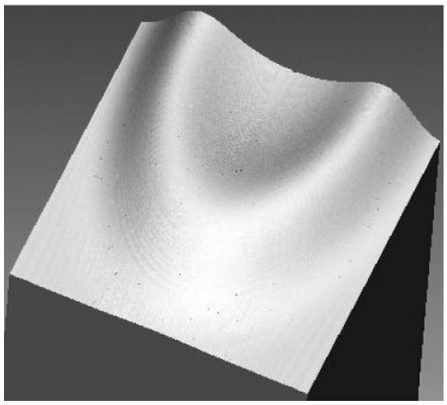

(i) Virtual machining $VFAP_R$, fine cut

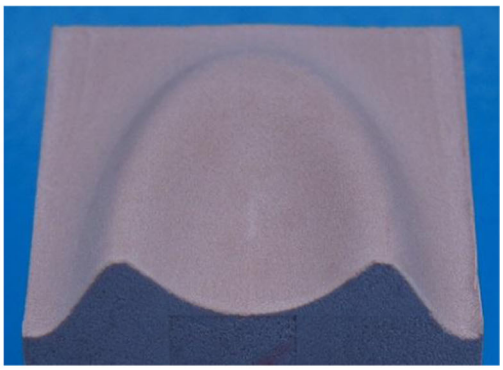

(j) Real machining $VFAP_R$, fine cut,
tool path length = 22676.7 mm (**advantage 13.8%**),
time = 1:03:59 hrs (**advantage 76.1%**)

Fig. 20 (continued)

machining path has been employed in order to minimize the tool wear during the rough machining. The finishing strategy employs $VFAP_R$ which maximizes the material removal rate and reduces the machining time. We observed that most of the time, the tool is moving along the direction of the minimal curvature.

The parametric region is decomposed into several subregions taking into account the direction of the vector field. Such decomposition can be performed manually or using vector field clustering [26]. In our particular case, the important points belong to a semi-circular region shown in Fig. 18b. The tool path in the remaining region does not generate large errors. Therefore, we partition the parametric region into two subregions and construct the required curvilinear grid in each subregion independently (see Fig. 19a). The BSFCs for the rough and fine cuts constructed from the curvilinear grid are shown in Fig. 19b–e, respectively. Note that in this particular case, we use a single-grid G_{LR} so that one family of the grid lines is used for $VFAP_L$ and another for $VFAP_R$.

The virtual and the real machining are presented in Fig. 20. The optimized tool path tested against the benchmark algorithms is presented in Table 6. The length of $VFAP_L$ path based on the adaptive grid technology is shorter by 7–20 %. For instance, when the maximum allowable scallop height h= 0.05, the length of the tool path is about 2500 mm shorter. The machining time for the fine cut using $VFAP_R$ has been reduced by 76 %. In other words, the proposed method reduces the machining time by (approximately) factor 2.

There is a clear advantage relative to UG. For instance, MAHO 600 E for h=0.25 the $VFAP_R$ requires 39 min vs. 1 h and 42 min using UG-FP and 18 h and 57 min using UG-HS(see the full evaluation in Table 6).

Table 7 compares the quality of the proposed method vs. the ISO path in terms of kinematic error and the number of the required CC points. Clearly, the error stays within the prescribed limits whereas the number of the CC points has been drastically reduced for high accuracy milling (h=0.1 and h=0.01).

Table 6 VFAP vs. conventional tool paths. Surface 3

Tool radius 4 mm			Tool path generation method		Scallop height(mm)			
					Roughing			Finishing
					0.25	0.1	0.05	0.01
Performance	Tool path length (mm)		Master CAM		35,553.0	72,215.0	128,879.0	–
			UG	HS	25,991.0	62,825.0	125,070.0	640,866.0
				FP	5480.4	8115.6	11,175.0	24,150.0
			ISO zigzag		5755.2	8666.1	12,034.0	26,305.0
			$VFAP_L$		5336.9	7092.7	9545.7	20,819.8
			$VFAP_R$		5489.1	7601.2	10,075.0	22,676.7
	Machining Time	MAHO 600 E	UG	HS	2:03:53.1	4:57:21.7	9:52:27.2	18:57:04.1
				FP	0:22:15.4	0:33:09.6	0:46:22.0	1:42:32.4
			ISO zigzag		0:28:22.1	0:43:39.8	1:01:03.8	2:14:50.2
			$VFAP_L$		0:27:14.5	0:41:20.4	0:56:19.7	2:00:41.2
			$VFAP_R$		0:10:25.4	0:14:21.7	0:19:22.9	0:39:19.1
		Haas VF-2TR	UG	HS	3:26:00.6	8:13:54.1	16:22:50.4	29:54:09.1
				FP	0:45:04.7	1:07:20.4	1:33:35.8	3:24:28.2
			ISO zigzag		0:56:13.9	1:26:37.5	2:01:03.5	4:27:22.0
			$VFAP_L$		0:55:09.7	1:24:21.2	1:55:52.1	4:08:22.3
			$VFAP_R$		0:17:46.1	0:24:56.1	0:33:36.1	1:03:58.7
Advantage rel. to ISO	Tool path length (mm)		$VFAP_L$		7.3 %	18.2 %	20.7 %	20.9 %
			$VFAP_R$		4.6 %	12.3 %	16.3 %	13.8 %
	Machining Time	MAHO 600 E	$VFAP_L$		4.0 %	5.3 %	7.8 %	10.5 %
			$VFAP_R$		63.3 %	67.1 %	68.3 %	70.8 %
		Haas VF-2TR	$VFAP_L$		1.9 %	2.6 %	4.3 %	7.1 %
			$VFAP_R$		68.4 %	71.2 %	72.2 %	76.1 %

Table 7 Kinematic error. VFAP vs. conventional tool paths. Surface 3

	Tool path generation method		Hausdorff distance											
			Roughing									Finishing		
			h=0.25			h=0.10			h=0.05			h=0.01		
			#CC	Ave	Std	#CC	Ave	Std	#CC	Ave	Std	#CC	Ave	Std
MAHO 600 E	UG	HS	3806	0.040	0.059	19,262	0.025	0.024	62,482	0.017	0.012	210,745	0.005	0.003
		FP	1663	0.040	0.054	7152	0.026	0.024	14,921	0.019	0.014	57,320	0.005	0.003
	ISO zigzag		5047	0.064	0.063	9334	0.038	0.025	16,652	0.022	0.012	68,889	0.005	0.002
	$VFAP_L$		4059	0.054	0.002	9059	0.022	0.025	16,773	0.012	0.013	65,186	0.003	0.002
	$VFAP_R$		5374	0.009	0.004	7151	0.009	0.001	9331	0.009	0.001	29,288	0.003	0.001
Haas VF-2TR	UG	HS	6295	0.053	0.062	29,996	0.032	0.026	102,859	0.019	0.012	312,345	0.005	0.002
		FP	3406	0.053	0.062	7091	0.033	0.028	18,016	0.019	0.013	95,136	0.005	0.002
	ISO zigzag		5882	0.082	0.064	10,299	0.040	0.024	18,603	0.023	0.012	83,202	0.005	0.002
	$VFAP_L$		4321	0.065	0.006	9418	0.025	0.026	17,437	0.013	0.013	68,075	0.003	0.002
	$VFAP_R$		5378	0.013	0.010	7157	0.013	0.008	9625	0.011	0.004	32,515	0.004	0.001

Table 8 Roughness and Waviness of VFAP-BSFC vs. conventional tool paths. Surface 3

	Roughness R_α (μm)			Standard deviation			Waviness (μm)			Standard deviation		
Machining stage	ISO zigzag	$VFAP_L$	$VFAP_R$	ISO zigzag	$VFAP_L$	$VFAP_R$	ISO zigzag	$VFAP_L$	$VFAP_R$	ISO zigzag	$VFAP_L$	$VFAP_R$
Rough cut	8.1	7.8	6.8	10.5	8.1	3.1	31.9	17.8	12.2	7.5	6.2	1.5
Finishing	7.3		7.1	10.2		9.1	14.0		10.7	4.1		0.7

Table 8 shows the quality of machined surface for the rough and finishing cuts evaluated by the stylus profiling. The rough cut by $VFAP_L$ has slightly better quality compared to ISO zigzag, 7.8 vs. 8.1 μm. Waviness produced by $VFAP_L$ is much lower, 17.8 vs. 31.9. Similarly, the fine-cut $VFAP_R$ is characterized by a slightly better quality 7.0 vs. 7.3 μm and the improved waviness: 10.7 vs. 14.0 μm. We hypothesize that the improved waviness is due to a reduced variation of the rotation angles. However, the main advantage of the method is the reduction of the length of the tool path and the machining time while keeping the same quality of the part surface.

Finally, since the proposed trajectory requires iterative calculations, the computational time might be a concern. Therefore, Table 9 compares the computational time of the proposed methods with the benchmark algorithms and the machining time. The proposed algorithm implemented in MATLAB (some libraries have been compiled from C) works slower than the benchmark methods; however, the computational time is only several minutes. The largest computational time is 10 min for h=0.01 (about 10,000 CC points). Note that translating the entire code from MATLAB into C usually decreases the computational time by factor 3–10.

8 Conclusions

A new method for generation of vector field-aligned tool paths for 5-axis machining has been presented and analyzed. The new idea is the numerical generation of a curvilinear grid adapted to the vector field of optimal directions and the biased space-filling curve. The method provides up to 70 % decrease of the machining time with regard to the iso-parametric tool path, works better than preceding methods based on the non biased space-filling curves, and outperforms advanced tool path generation methods developed by MasterCAM and Unigraphics. The tests against the benchmark methods show that the kinematic error and the roughness of the workpiece remain practically unchanged, while the machining time, the tool path length, and the waviness have been considerably reduced.

Table 9 Computational time vs. the machining time

Test	Scallop height (mm)	Computational time (min)					Machining time (min)			
		Master CAM	UG		MATLAB/C		MAHO 600 E		Haas VF-2TR	
		Zigzag	HS	FP	Zigzag	VFAP	Zigzag	VFAP	Zigzag	VFAP
Surface 1	0.25	1	1	1	1	3	28	18	45	33
	0.10	1	8	2	1	4	44	28	72	52
	0.05	1	30	2	1	5	64	40	103	74
Surface 2	0.25	1	1	1	1	6	8	6	33	26
	0.10	1	1	1	1	8	12	9	53	41
	0.05	1	3	1	1	10	17	13	75	56
Surface 3	0.25	1	1	1	1	2	28	10	56	17
	0.10	1	3	1	1	2	43	14	86	24
	0.05	1	27	1	1	2	61	19	121	33
	0.01	1	54	1	1	2	134	39	267	63

Acknowledgments This research is supported by the Thailand Research Fund through the Royal Golden Jubilee Scholarship (Grant no. PHD/0330/2551).

Appendix A. Space-filling curves

The rectangular grid in (ξ,η) is treated as an undirected graph whereas tool path generation on the grid-like graph is a Hamiltonian path problem. All grid cells (graph nodes) are covered by small disjoint circuits (see Fig. 21). The circuits are then merged into a single Hamiltonian circuit. The initial circuits are created by constructing rectangular cyclic paths over every four adjacent vertices, i.e., by connecting the vertices on even rows and columns with the vertices on odd rows and columns, respectively, as shown in Fig. 21. If the number of rows or columns is odd, additional virtual circuits are created along the boundaries (dashed lines in Fig. 21). Any two adjacent circuits can be merged into one bigger circuit. The cost of merging is defined by maximum material removal rate (see section Biased Space-Filling Curve).

All virtual circuits are initially merged. This is to ensure that there is no discontinuity of the tool path after removing

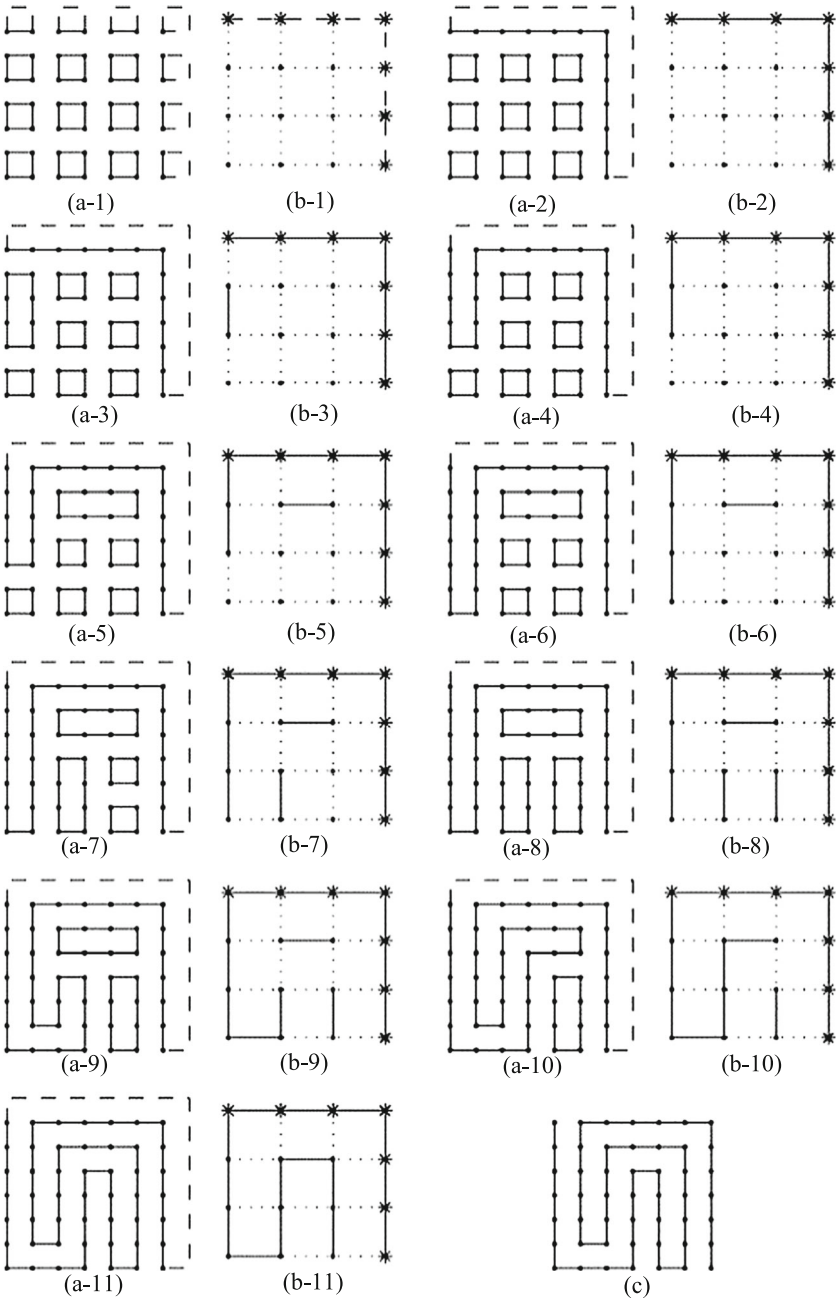

Fig. 21 Construction of the space-filling curve

the virtual edges from the Hamiltonian path. Furthermore, a non-virtual circuit A can be merged with a virtual circuit D only if A is merged with a non-virtual circuit C located on the opposite side. To enforce this merging dependency, the cost of merging A and D is set equal to that of merging A and C. The merging dependency is used to eliminate a possibility of an inappropriate narrow zigzag with a large number of turns along the boundaries.

Next, we construct a dual graph G' where each small circuit in G corresponds to a vertex in G'.

Finally, a minimum spanning tree is constructed by iteratively merging circuits using the proposed cost function. When all circuits are merged into the Hamiltonian path, the SFC is obtained by removing all virtual edges. Figure 21 illustrates the algorithm.

Appendix B. List of basic notations

VFAP	Vector field-aligned path
VFAP_R	Vector field-aligned path based on the material removal rate
VFAP_L	Vector field-aligned path based on the length of the tool path
SFC	Space-filling curve
BSFC	Biased space-filling curve
UG-FP	Tool path of Unigraphics, option "Follow Periphery"
UG-HS	Tool path of Unigraphics, option "Helical or Spiral"
CC point	Cutter contact point
CL point	Cutter location point
(u,v)	Parametric coordinates
(ξ,η)	Computational coordinates
$u(\xi,\eta), v(\xi,\eta)$	Curvilinear grid
t	A parameter along the trajectory (pseudo time)
X,Y,Z	Machine coordinates
x,y,z	Workpiece coordinates
$S(u,v)$	Part surface
A,B	Rotation matrices corresponding to the two rotary axes
$(a\ b)$	Rotation angles
T_{23}	The origin of the A-axis in the B-axis coordinate system
T_{34}	The origin of the B-axis in the spindle coordinate system
L	Length of the tool
(I_x,I_y,I_z)	Tool orientation vector
W	A point on the surface
$R_M(W)$	Material removal rate
$V(u,v)$	Vector field of the optimal directions
$(\alpha(u,v),\beta(u,v))$	Dual vector field $((\alpha(u,v)\cup\beta(u,v)=V(u,v)))$
F_S	Smoothness functional
F_A	Alignment functional
λ	Weighting coefficient
$W^D_{p,p+1}(t)$	Space curve on the surface between tool positions W_p and W_{p+1}
dist_H	Hausdorff distance
$\mathfrak{K}$	Kinematic transformation
w_L,w_R	The left and the right machining strip
h	Maximum allowable scallop height (accuracy)
ε	Kinematics error

References

1. Lo CC (1999) Efficient cutter-path planning for five-axis surface machining with a flat-end cutter. Comput Aided Des 31(9):557–566
2. Rao A, Sarma R (2000) On local gouging in five-axis sculptured surface machining using flat-end tools. Comput Aided Des 32(7): 409–420
3. Hopcroft JE, Ullman JD (1979) Introduction to automata theory, languages, and computation. Addison-Wesley
4. Griffiths JG (1994) Toolpath based on Hilbert's curve. Comput Aided Des 26(11):839–844
5. Tarbutton J, Kurfess TR, Tucker T, Konobrytskyi D (2013) Gouge-free voxel-based machining for parallel processors. Int J Adv Manuf Tech 69(9–12):1941–1953
6. Cox JJ, Takezaki Y, Ferguson HRP, Kohkonen KE, Mulkay EL (1994) Space-filling curves in tool-path applications. Comput Aided Des 26(3):215–224
7. He W, Lei M, Bin HZ (2009) Iso-parametric CNC tool path optimization based on adaptive grid generation. Int J Adv Manuf Tech 41(5–6):538–548
8. Lin ZW, Fu JZ, Shen HY, Gan WF (2014) An accurate surface error optimization for five-axis machining of freeform surfaces. Int J Adv Manuf Tech 71(5–8):1175–1185
9. Anotaipaiboon W, Makhanov SS (2003) Tool path generation for five-axis NC machining using space-filling curves. In Proceedings of The Third Asian Conference on Industrial Automation and Robotics
10. Sun Y, Ren F, Zhu X, Guo D (2012) Contour-parallel offset machining for trimmed surfaces based on conformal mapping with free boundary. Int J Adv Manuf Tech 60(1–4):261–271
11. Dolen M, Yaman U (2014) New morphological methods to generate two-dimensional curve offsets. Int J Adv Manuf Tech 71(9–12): 1687–1700
12. Can A, Unuvar A (2010) A novel iso-scallop tool-path generation for efficient five-axis machining of free-form surfaces. Int J Adv Manuf Tech 51(9–12):1083–1098
13. Anotaipaiboon W, Makhanov SS (2005) Tool path generation for five-axis NC machining using adaptive space-filling curves. Int J Prod Res 43(8):1643–1665
14. Anotaipaiboon W, Makhanov SS, Bohez EJ (2006) Optimal setup for 5-axis machining. Int J Mach Tools Manuf 46:964–977
15. Gao J, Chen X, Zheng D, Yilmaz O, Gindy N (2006) Adaptive restoration of complex geometry parts through reverse engineering application. Adv Eng Softw 37(9):592–600

16. Lee Y-S (1997) Admissible tool orientation control of gouging avoidance for 5-axis complex surface machining. Comput Aided Des 29(7):507–521
17. Lin ZW, Shen HY, Gan WF, Fu JZ (2012) Approximate tool posture collision-free area generation for five-axis CNC finishing process using admissible area interpolation. Int J Adv Manuf Tech 62(9–12):1191–1203
18. Du J, Yan XG, Tian XT (2012) The avoidance of cutter gouging in five-axis machining with a fillet-end milling cutter. Int J Adv Manuf Tech 62(1–4):89–97
19. Yoon J-H (2003) Tool tip gouging avoidance and optimal tool positioning for 5-axis sculptured surface machining. Int J Prod Res 41(10):2125–2142
20. Lee Y-S (1998) Non-isoparametric tool path planning by machining strip evaluation for 5-axis sculptured surface machining. Comput Aided Des 30(7):559–570
21. Lee YS (1998) Mathematical modelling using different endmills and tool placement problems for 4- and 5-axis NC complex surface machining. Int J Prod Res 36(3):785–814
22. Chiou C-J, Lee Y-S (2002) A machining potential field approach to tool path generation for multi-axis sculptured surface machining. Comput Aided Des 34(5):357–371
23. Kim T, Sarma SE (2002) Toolpath generation along directions of maximum kinematic performance; a first cut at machine-optimal paths. Comput Aided Des 34(6):453–468
24. Dong J, Ferreira PM, Stori JA (2007) Feed-rate optimization with jerk constraints for generating minimum-time trajectories. Int J Mach Tools Manuf 47(12–13):1941–1955
25. My CA, Bohez ELJ, Makhanov SS (2005) Critical point analysis of 3D vector field for 5-axis tool path optimization. In Proceedings of the 4th Asian Conference on Industrial Automation and Robotics ACIAR :11–13
26. Makhanov S (2007) Optimization and correction of the tool path of the five-axis milling machine: part 1. Spatial optimization. Math Comput Simulat 75(5–6):210–230
27. Park SC, Chung YC (2002) Offset tool-path linking for pocket machining. Comput Aided Des 34(4):299–308
28. Li LL, Zhang YF, Li HY, Geng L (2011) Generating tool-path with smooth posture change for five-axis sculptured surface machining based on cutter's accessibility map. Int J Adv Manuf Tech 53(5–8):699–709
29. Munlin M, Makhanov SS, Bohez ELJ (2004) Optimization of rotations of a five-axis milling machine near stationary points. Comput Aided Des 36(12):1117–1128
30. Makhanov SS (1999) An application of variational grid generation techniques to the tool-path optimization of industrial milling robots. Comput Math Math Phys 39(9):1524–1535
31. Makhanov SS, Ivanenko SA (2003) Grid generation as applied to optimize cutting operations of the five-axis milling machine. Appl Numer Math 46(3–4):331–351
32. Bohez E, Makhanov SS, Sonthipermpoon K (2000) Adaptive nonlinear tool path optimization for five-axis machining. Int J Prod Res 38(17):4329–4343
33. Bieterman MB, Sandstrom DR (2003) A curvilinear tool-path method for pocket machining. J Manuf Sci Eng 125(4):709–715
34. Thompson JF, Soni BK, Weatherill NP (1998) Handbook of grid generation. CRC Press
35. Ivanenko SA (1988) Generation of non-degenerate meshes. USSR Comput Math Mathemat Phys 28(5):141–146
36. Anotaipaiboon W, Makhanov SS (2011) Minimization of the kinematics error for five-axis machining. Comput Aided Des 43(12):1740–1757
37. Makhanov SS, Anotaipaiboon W (2007) Advanced numerical methods to optimize cutting operations of five axis milling machines. Springer,
38. Castillo JE, Otto JS (2000) Numerical techniques for the transformation to an orthogonal coordinate system aligned with a vector field. Comput Math Appl 40(4–5):523–535
39. Brackbill JU, Saltzman JS (1982) Adaptive zoning for singular problems in two dimensions. J Comput Phys 46(3):342–368
40. Giannakopoulos AE, Engel AJ (1988) Directional control in grid generation. J Comput Phys 74(2):422–439
41. Winslow AM (1966) Numerical solution of the quasilinear Poisson equation in a nonuniform triangle mesh. J Comput Phys 1(2):149–172
42. Anotaipaiboon W, Makhanov SS (2008) Curvilinear space-filling curves for five-axis machining. Comput Aided Des 40(3):350–367
43. Vorburger TV, Raja J (1990) Surface finish metrology tutorial. National Inst. of Standards and Technology,
44. Tabenkin A (1988) Function: the key to surface finish requirements. In Proc of 4th Biennial International Manufacturing Technology Conference Session 8. NMTBA McLean VA
45. ASME/ANSI (American Society of Mechanical Engineers/American National Standards Institute), ASNI B46.1 (1985) Surface texture. American Society of Mechanical Engineers, New York
46. Gaspar M, Weichert F (2013) Integrated construction and simulation of tool paths for milling dental crowns and bridges. Comput Aided Des 45(10):1170–1181